Molecular model of a bacterial flagellar motor *in situ* reveals a "parts-list" of protein adaptations to increase torque

Tina Drobnič[1,2,3,£], Eli J. Cohen[1,4,£], Tom Calcraft[18], Mona Alzheimer[5,6], Kathrin Froschauer[5,7], Sarah Svensson[5,8,9], William H. Hoffmann[21,22], Nanki Singh[1], Sriram G. Garg[10,11], Louie Henderson[1,12], Trishant R. Umrekar[1], Andrea Nans[13,14], Deborah Ribardo[15], Francesco Pedaci[21,23], Ashley L. Nord[21,24], Georg K. A. Hochberg[11], David R. Hendrixson[15,16], Cynthia M. Sharma[5,17], Peter B. Rosenthal[18,19], Morgan Beeby[1,20,*]

[1]Department of Life Sciences, Imperial College London, London, SW7 2AZ, UK

[2]ORCID: 0000-0001-6364-1874

[3]Tina Drobnič current affiliation: MRC Laboratory of Molecular Biology, Francis Crick Avenue, Cambridge CB2 0QH, UK.

[4]ORCID: 0000-0001-9265-7517

[5]University of Würzburg, Institute of Molecular Infection Biology, Department of Molecular Infection Biology II, Josef-Schneider-Straße 2/D15, 97080 Würzburg, Germany

[6]ORCID: 0000-0002-0094-3987

[7]ORCID: 0000-0001-5288-4440

[8]Current affiliation: The Center for Microbes, Development and Health, CAS Key Laboratory of Molecular Virology and Immunology, Institut Pasteur of Shanghai, Chinese Academy of Sciences, Shanghai, China 200031. email: sarah.svensson@ips.ac.cn

[9]ORCID: 0000-0002-3183-6084

[10]ORCID 0000-0003-4160-5228

[11]Max Planck Institute for Terrestrial Microbiology, Marburg, Germany

[12]Current affiliation: Peptone Ltd, 370 Grays Inn Road, London WC1X 8BB, UK

[13]Structural Biology Science Technology Platform, The Francis Crick Institute, London NW1 1AT, UK

[14]ORCID: 0000-0002-3791-2447

[15]Department of Microbiology, University of Texas Southwestern Medical Center, Dallas, TX 75390

[16]ORCID: 0000-0001-8496-2466

[17]ORCID: 0000-0002-2321-9705

[18]Structural Biology of Cells and Viruses Laboratory, The Francis Crick Institute, London NW1 1AT, UK

[19]ORCID: 0000-0002-0387-2862

[20]ORCID: 0000-0001-6413-9835

[21]Centre de Biologie Structurale, Universite de Montpellier, CNRS, INSERM. Mont-pellier, France

[22]ORCID: 0000-0002-6689-2609

[23]ORCID: 0000-0002-4530-3027

[24]ORCID: 0000-0001-6199-2769

[£]These authors contributed equally to this work

[*]Correspondence: mbeeby@imperial.ac.uk

Abstract

One hurdle to understanding how molecular machines work, and how they evolve, is our inability to see their structures *in situ*. Here we describe a minicell system that enables *in situ* cryogenic electron microscopy imaging and single particle analysis to investigate the structure of an iconic molecular machine, the bacterial flagellar motor, which spins a helical propeller for propulsion. We determine the structure of the high-torque *Campylobacter jejuni* motor *in situ,* including the subnanometre-resolution structure of the periplasmic scaffold, an adaptation essential to high torque. Our structure enables identification of new proteins, and interpretation with molecular models highlights origins of new components, reveals modifications of the conserved motor core, and explain how these structures both template a wider ring of motor proteins, and buttress the motor during swimming reversals. We also acquire insights into universal principles of flagellar torque generation. This approach is broadly applicable to other membrane-residing bacterial molecular machines complexes.

Introduction

How evolution innovates remains a fundamental question. While innovations in eukaryotes often arise by rewiring existing gene transcriptional networks[1], examples of the emergence of evolutionary novelty at the molecular scale remain scarce. The few case studies in the emergence of new molecular structures are limited to small protein complexes[2–5].

Bacterial flagella, helical propellers rotated by a cell-envelope-embedded rotary motor, are examplars of the emergence of molecular novelty[6] (Fig. 1A). The flagellum, best studied in model organisms *Salmonella enterica* serovar Typhimurium and *Escherichia coli*, is composed of a ring of inner-membrane motor proteins ("stator complexes") which harness ion flux to rotate a large cytoplasmic rotor ring (the "C-ring"). Torque is transmitted through a chassis (the "MS-ring") and periplasm-spanning axial driveshaft (the "rod") to an extracellular propeller structure that generates thrust. Structures of isolated C-ring[7,8], parts of stator complexes[9,10], MS-ring attached to the rod[11,12], and axial structures[13,14] have recently been determined.

Many flagellar motors have evolved diverse additional proteins associated with greater than the ~11 stator complexes seen in the model motors[15–17], likely explaining their associated higher torque. Some of the most complex motors are found in the Campylobacterota, a phylum that includes pathogens *Campylobacter jejuni* and *Helicobacter pylori*[16,18], which incorporate many additional proteins believed to contribute to three times higher torque generation than *E. coli* and *Salmonella*[17].

Comparisons of diverse Campylobacterota motors and contextualisation against the *C. jejuni* motor, the most-studied Campylobacterota motor, have suggested a stepwise evolutionary recruitment of proteins[17]. First, inner membrane-associated periplasmic proteins (PflA and PflB, from "Paralysed flagellum" proteins A and B) template assembly of a wider ring of the stator complex motor proteins[16]. This wider ring can exert greater leverage on the correspondingly-wider C-ring to produce the motor's substantially higher torque, an adaptation likely associated with the highly viscous gut mucous that many Campylobacterota species inhabit[16,18]. Independently, a large (~100 nm-wide) outer membrane-associated "basal disk" of protein FlgP evolved[16,17,19] that we recently found is needed for buttressing the motor while wrapping and unwrapping the flagellar filament from the cell body[20]. These structures have been suggested to have initially been independent, and subsequently become co-dependent upon for assembly[17], but the physical basis for this, and the origins of these new proteins, remains unclear.

88 Understanding how and why these additional proteins were incorporated into the motor, and
89 how they contribute to function, requires molecular-scale models, but the size, intimate
90 membrane association, and multiple moving parts have hampered structural determination.
91 Cryogenic electron microscopy (cryoEM) subtomogram average structures to between 16 and
92 18 Å-resolution[11,21], and structures of purified flagellar motors by single particle analysis
93 cryoEM lacking dynamic components[8,11,12] do not discern the molecular architecture of these
94 additional structures. Meanwhile advances in imaging membrane proteins *in situ* remain
95 restricted to spherical liposomes rather than native context[22,23].

96 To address these challenges, we engineered *C. jejuni* minicells for subnanometre-resolution
97 structure determination of the flagellar motor *in situ.* The quality of our map enabled us for the
98 first time to assemble a molecular model of its evolutionary elaborations. Our model provides
99 key insights into the contributions of new proteins, reveals distant homologies based on
100 structural comparisons, identifies previously unknown components, and contextualises
101 adaptations of pre-existing core machinery to these recruited proteins. We also gain insights
102 into the function of the conserved core of the flagellar motor.

103 Results

104 ***Projection imaging of bacterial minicells enables subnanometre***
105 ***resolution* in situ *structure determination***

106 To increase particle number for high-resolution structure determination, we exploited the
107 multiply-flagellated, still-motile minicell phenotype produced by a Δ*flhG* mutation[24], but
108 removed the flagellum by deleting filament proteins *flaA* and *flaB* for centrifugal purification
109 (Fig. 1B,C). The resulting ~200 nm-diameter minicells are more homogenous than ~350 nm-
110 diameter minicells from Enterobacteriaceael minicells such as *E. coli* and *Salmonella*[25]. The
111 polar curvature remains comparable to wildtype cells, meaning motor structures are
112 unperturbed (Fig. 1B,C).

113 We acquired micrographs of minicells for *in situ* single particle analysis. Initial 2-D
114 classification revealed features including the stator complexes and their periplasmic scaffold,
115 basal disk, C-ring, MS-ring, and rod (Fig. 1D). Classification and refinement applying the
116 established dominant C17 symmetry[16] yielded a reconstruction to 9.4 Å resolution using
117 32,790 particles (Fig. 1E, Extended Data Fig. 1). The 17-fold symmetric periplasmic structures
118 exhibited features consistent with discrete proteins, while symmetry-mismatched regions were
119 cylindrical averages of respective structures (Fig. 1E,F). Focused refinement of the

120 periplasmic region improved resolution to 7.9 Å (Fig. 2A; Extended Data Fig. 1D,E,F),
121 sufficient to resolve α-helices and β-sheets (Fig. 2A,B).

122 *The basal disk is composed of concentric rings of FlgP*

123 The basal disk forms a concave cup that pushes the outer membrane away from the inner
124 membrane at increasing distances from the motor (Fig. 2A). Knowing that the disk is
125 composed of FlgP and possibly FlgQ[16,19], we predicted monomeric and multimeric structures
126 of FlgP, excluding the N-terminal signal sequence and linker[19] to the outer membrane[20] using
127 AlphaFold[26] (Fig. 2A-D). Oligomers laterally associate to form a continuous β-sheet, with
128 interaction of one FlgP with the next two protomers. Bending the arc of these oligomers
129 demonstrated fit of 17 trimeric repeats of 51 protomers into the 51 periodic densities of the
130 inner ring of the basal disk, with a map-model FSC of 9.9 Å at FSC = 0.5 (Fig. 2A-D, Extended
131 Data Fig. 2A, 3A). Each trimeric repeat also featured an additional medial disk-facing density
132 (Fig. 2A,B,C). Although we could not discern the symmetries of rings beyond the 51-fold
133 symmetry of the first, assembly of the disk is entirely reliant upon *flgP*[16]. Subsequent rings all
134 have comparable cross-section densities, making them very unlikely to be composed of a
135 protein other than FlgP. Based on ratios of circumferences, we predict each subsequent ring
136 incorporates 11 additional protomers, explaining the symmetry mismatch with the 17-fold
137 symmetric structures (Fig. 2E).

138 The FlgP fold is a modified SHS2 domain from InterPro family IPR024952, with a three-
139 stranded β-sheet and an α-helix spanning one face[27] (Fig. 2F). Structural searches revealed
140 this fold is also present in γ-proteobacterial FlgT, a flagellar component from sodium-driven
141 flagellar motors, and *Helicobacter* Lpp20[28] (Fig. 2F). FlgP, however, features an additional
142 short C-terminal helix and a long β-hairpin between the α-helix and second β-sheet that
143 extends 35 Å at a ~42° angle to the vertical axis; it is this β-hairpin that forms the continuous
144 β-sheet in the inner face of each FlgP concentric ring.

145 FlgQ occurs in an operon with FlgP, is outer membrane-localized, and required for FlgP
146 stability[19]. Its predicted structure resembles a two-protomer FlgP repeat (Fig. 2G). To clarify
147 its location we fused an mCherry tag to FlgQ and determined a subtomogram average
148 structure. Although the mutant was motile, the structure featured no additional densities (Fig.
149 2H), and we surmise that FlgQ is a low-abundance or irregular component, or an assembly
150 chaperone.

151 The basal disk is adjacent to the outer face of the P-ring. While ascertaining the symmetry of
152 the L- and P-rings was beyond the resolution of our map, cross-sections through L- and P-ring

153 densities showed comparable radii to *Salmonella*[11,12] (Fig. 2I). To understand the relationship
154 of the LP-rings to the basal disk, we cylindrically-averaged our map by applying arbitrary high-
155 order symmetry during focused refinement. We then compared these to low-pass filtered
156 structures of similarly cylindrically averaged *Salmonella* LP-rings. The *C. jejuni* L- and P-ring
157 diameters are approximately 103% and 104% those of *Salmonella*, respectively (Fig. 2I), and
158 the lack insertion and deletions, suggested comparable stoichiometries. To experimentally
159 probe the *C. jejuni* LP-ring stoichiometries, we looked for steps in flagellar rotation like the 26
160 steps imposed by interactions between the asymmetric rod and 26-fold symmetric *Salmonella*
161 and *E. coli* LP-rings[11]. We attached beads to truncated flagella, and upon slowing rotation by
162 de-energizing cells with CCCP, observed 25 to 27 phase-invariant dwell positions (Fig. 2J,
163 Extended Data Fig. 4). Taking these structural and biophysical observations together, we
164 conclude that the *C. jejuni* LP-rings have not expanded to match the symmetry of the basal
165 disk or other novel components, and have a symmetry similar to the 26-fold symmetry of the
166 *Salmonella* LP-rings.

167 We did not see evidence of YecR, which in *Salmonella* forms a belt around the LP-rings[11], nor
168 find a homolog in the *C. jejuni* genome, although an unidentified adjacent density hints at an
169 as-yet-unidentified analog (Fig. 2I).

170 Although our density maps show close association of the P-ring with the basal disk, the basal
171 disk can assemble even when pushed out of axial register with the P-ring by increasing the
172 length of the FlgP N-terminal linker[20]. This indicates that the basal disk does not directly
173 template upon the P-ring, despite their proximity.

174 *The medial disk is a lattice of PflC with PflD*

175 The medial disk, a lattice between the basal and proximal disks (Fig. 3A), is of unknown
176 composition. An unpublished Tn-seq based infection screen using *C. jejuni* NCTC11168
177 (Alzheimer, Svensson, Froschauer, Sharma, in preparation) revealed proteins Cj1643 and
178 Cj0892c are required for motility and are polarly-localised, but are not required for flagellar
179 filament assembly, suggesting them as peripheral motor components. Co-
180 immunoprecipitation with proximal disk component PflA in *C. jejuni* 81-176 recovered
181 orthologs CJJ81176_1634 and CJJ81176_0901, respectively (Table S1), which we renamed
182 PflC and PflD (Paralysed flagellum C and D). Subtomogram average structures of deletion
183 mutants (Fig. 3B) revealed loss of the proximal and medial disks upon deletion of *pflC* and
184 loss of a peripheral cage-like structure between the medial and proximal disks upon deletion
185 of *pflD*.

186 PflC is a 364-residue periplasmic protein featuring N-terminal serine protease and PDZ-like
187 domains ($PflC_N$, residues 16-252), a proline-rich linker, and a second PDZ-like domain ($PflC_C$,
188 residues 265-364). By rigid-body docking of $PflC_N$ and $PflC_C$ we located seventeen copies of
189 PflC in the densities projecting from each third FlgP subunit of the first basal disk ring, yielding
190 a map-model FSC of 9.3 Å at FSC = 0.5 (Fig. 3C, Extended Data Fig. 2A, 3B). This domain
191 arrangement resembles trypsin-like HtrA serine proteases[29] (Fig. 3D), albeit lacking the
192 catalytic residues (Extended Data Fig. 5A,C). $PflC_C$ binds FlgP, while $PflC_N$ forms the inner
193 band of the medial disk; a density corresponding to the linker links adjacent PflC protomers,
194 revealing that the $PflC_C$ domain of one chain assembles with the $PflC_N$ domain of another in a
195 daisy-chain of domain-swapped protomers (Fig. 3C). PDZ domains interface with binding
196 partners via a hydrophobic pocket using β-strand addition, but $PflC_C$ interactions are unlikely
197 to be mediated by canonical binding[30] as its ligand-binding groove is oriented away from FlgP,
198 lacks the conserved binding loop[31], and is predicted to be occupied by residues from its own
199 chain.

200 The remainder of the medial disk is a lattice of α-helical densities. The resolution was sufficient
201 for us to see that it is composed of six additional $PflC_N$ subunits related by diverse dimerization
202 interfaces (Fig. 3E). The $PflC_N$ subunits could be docked into our density map with a map-
203 model FSC of 9.7 Å at FSC = 0.5 (Extended Data Fig. 2A, 3C). We refer to the subunits in one
204 asymmetric unit as $PflC_{2-7}$; $PflC_{2-6}$ form radial spokes with a slight twist, while $PflC_7$ connects
205 spokes. Validating our assignment of PflC, we noted an additional rodlike density protruding
206 from the location of N239 in all PflCs, which in a closely-related species is glycosylated with
207 an N-linked heptasaccharide[32]. Pulldowns using FLAG-tagged PflC verified the interactions
208 with FlgP and proximal disk components PflA and PflB evident in our map (Fig. 3F).

209 The PflC lattice consists of diverse oligomerisation interfaces (Fig. 3G,H). There are three
210 types of symmetric dimerisation interfaces with rotational axes perpendicular to the plane of
211 the lattice: one is present in $PflC_2$:$PflC_3$ and $PflC_4$:$PflC_5$; one in $PflC_3$:$PflC_4$ and $PflC_5$:$PflC_6$;
212 and a third in $PflC_3$:$PflC_7$, although the latter is substantially distorted. The remaining interfaces
213 ($PflC_1$:$PflC_1$, $PflC_1$:$PflC_2$, $PflC_2$:$PflC_7$, and $PflC_7$:$PflC_4$) are asymmetric and differ in each case.
214 Based on our findings with $PflC_1$, the densities on the underside of the basal disk are likely the
215 C-terminal PDZ domains of $PflC_{2-7}$ (asterisks in Fig. 2A, opaque teal in 3A), although the lack
216 of C17 symmetry renders linker helices invisible.

217 These promiscuous self-self interfaces predicted that PflC would oligomerise *ex situ*.
218 Curiously, size exclusion chromatography (Extended Data Fig. 5Ei,ii) and mass photometry
219 (Extended Data Fig. 5Eiii) of heterologously expressed PflC indicated a dimer. The *in situ*
220 $PflC_N$-$PflC_C$ daisy-chaining suggests that the two domains of discrete PflC polypeptides might

221 self-associate, reducing the abundance of the dimer. To test this, we removed $PflC_C$. $PflC_N$
222 produced dimers that were more abundant than full-length PflC dimers (Extended Data Fig.
223 5iv-vi). We speculate that interaction of $PflC_N$ and $PflC_C$ from the same polypeptide prevents
224 cytoplasmic oligomerization, and binding of $PflC_C$ to the basal disk catalyzes assembly of the
225 medial disk only in the context of the assembled motor.

226 The second candidate medial disk component, PflD, is a 162-residue periplasmic protein that
227 pulls down with PflA of the proximal disk (Table S1). We inspected the peripheral part of the
228 medial disk adjacent to $PflC_{4N}$ which disappeared when we deleted *pflD*, and found that a
229 model of PflD was consistent with this density, despite the lower resolution of this area of our
230 map yielded only a modest mean main chain correlation coefficient of 0.63 (Fig. 3I, Extended
231 Data Fig. 2B).

232 *PflA spokes, a rim of PflB, and 17 arcs of FliL make the proximal disk*

233 Finally, we sought to interpret our density map of the proximal disk, known to contain PflA and
234 PflB, together with stator complex protein MotB[16]. This region features the extensive short
235 antiparallel α-helical motifs characteristic of the repetitive TPR motifs[33,34] predicted for proximal
236 disk components PflA and PflB (Fig. 4A). PflA is predicted to form an elongated superhelix
237 consisting of 16 TPR motifs connected to an N-terminal β-sandwich domain by an unstructured
238 linker. Meanwhile PflB is predicted to be α-helical except two five-residue β-strands. We
239 flexibly fitted these structures into our map, with reference to the predicted structure of a PflAB
240 heterodimer (Extended Data Fig. 3D), with 17 radial spokes of PflA positioning a continuous
241 rim of 17 PflBs (Fig. 4B). PflA fitted the map with a map-model FSC of 9.1 Å at FSC = 0.5
242 (Extended Data Fig. 2A). The resolution of PflB was lower, presumably because it is more
243 peripheral and therefore more flexible, with map-model mean main chain correlation
244 coefficient of 0.71 (Extended Data Fig. 2B).

245 PflAB heterodimer formation is mediated by a the PflA linker binding a TPR-superhelical
246 groove in PflB, with the α-helical PflA spoke pointing toward the motor axis, and the β-
247 sandwich domain wrapping around PflB (Fig. 4C). To verify this model we measured their
248 interaction using mass photometry. PflAB heterodimerised even at nanomolar concentrations
249 (Fig. 4E), while deleting the linker and β-sandwich domain of PflA (residues 16-168) abolished
250 dimer formation (Fig. 4F, Extended Data Fig. 6). A subtomogram average structure of the
251 motor in a $PflA_{\Delta 16\text{-}168}$ mutant confirmed that PflB was unable to assemble into the motor (Fig.
252 4E), although the C-terminal end of PflA remained evident, unlike a *pflA* deletion mutant[16] (Fig.
253 4G). Together with PflAB interaction seen in pulldowns[35], we conclude that PflAB dimerisation
254 is essential for completion of proximal disk assembly.

255 Our positioning of PflA is further validated by two additional rodlike densities protruding from
256 the midpoint of each PflA superhelix. Like PflC, PflA is a glycoprotein, with N-linked glycans
257 attached at N458 and N497[36], and these residues are situated at the base of the likely N-linked
258 heptasaccharide densities (Fig. 4C, red atoms).

259 An arc of density partially encircling the periplasmic MotB linker had similar radius and location
260 as the tertiary structures of complete circles of FliL in other motors[37,38], and we found that a
261 curved tetrameric homology model of FliL fitted into this arc with a mean main chain correlation
262 coefficient of 0.61 (Fig. 4D, Extended Data Fig. 2B). Co-immunoprecipitation assays confirmed
263 that FliL is found in pulldowns of PflA and PflB (Table S1), suggesting that the FliL arc is
264 augmented by PflB and PflA to scaffold MotB and explains why PflA and PflB are both required
265 for the high occupancy or static anchoring of stator complexes into the *C. jejuni* motor[16].
266 Indeed, we found that deletion of *fliL* in *C. jejuni* had only a modest impact upon motility (Fig.
267 4D) in contrast to *H. pylori* where FliL is essential, reinforcing that FliL's role is partially fulfilled
268 by PflA and PflB in *C. jejuni*. The presence of the stator complexes in the *C. jejuni* structure,
269 in contrast to their absence in *Salmonella,* indicates either high occupancy or static anchoring,
270 possibly mediated by their interactions with PflA, PflB, FliL, and potential cytoplasmic proteins.
271 Although our previous work and the topology of MotB make its location unambiguous, the
272 resolution of this region was low, meaning we could only crudely position a MotB model.

273 We could not assign proteins to three remaining densities in the scaffold: the so-called E-ring
274 that spaces the MS-ring from PflA, a cage previously observed in *H. pylori*[37] on the periphery
275 of the PflB rim that extends through the membrane to wrap around the stator complexes, and
276 a small density adjacent to PflD (Fig. 4A, opaque regions, single, double, and triple asterisks
277 respectively).

278 *Conserved motor components have adapted to a high torque role*

279 To better understand the flagellar torque-generation machinery we focused on the stator
280 complexes, C-ring, and MS-ring. By symmetry expanding and classifying stator complexes
281 from our whole-motor map, we observed a pentameric structure directly beneath the
282 periplasmic peptidoglycan-binding domain of MotB that contacts the C-ring (Fig. 5A,B,C). In
283 cross-section, the dimensions and shape of this density match that of purified *C. jejuni* stator
284 complex membrane component $MotA_5$[10] (Fig. 5C). The consistent rotational register of this
285 pentameric density even after symmetry expansion and classification, with a pentameric
286 corner pointing toward the C-ring, indicates that stator complexes are most frequently in this
287 rotational register.

288 We wondered how the *C. jejuni* rotor components, i.e., the C-ring, MS-ring, and rod, have
289 adapted to interact with a wider ring of stator complexes. The *C. jejuni* C-ring is wider than
290 that of *Salmonella*[16]*;* to ascertain its stoichiometry, we determined its structure by
291 subtomogram averaging. To remove the strong 17-fold signal of MotA, we used a motile *C.*
292 *jejuni* mutant whose stator complexes have lower occupancy than WT motors. Our
293 subtomogram average revealed a 38-fold periodic structure whose vertical post-like
294 architecture resembles that of the near-atomic-resolution *Salmonella* C-ring[8] (Fig. 5D,E,F).

295 C-ring diameter is reliant upon templating on the C-terminus of the MS-ring protein FliF[8,39]. To
296 examine possible mechanisms behind templating a wider C-ring, we compared the *C. jejuni*
297 MS-ring to that from *Salmonella.* The distinctive FliF β-collar has a radius of approximately 51
298 Å (Fig. 5G). Focused refinement of the *C. jejuni* MS-ring with imposed C38 symmetry expected
299 from 1:1 stoichiometry of FliF and FliG[39,40] demonstrated a 62 Å-radius FliF β-collar (Fig. 5H).
300 We could not resolve azimuthal features corresponding to discrete FliF subunits, but
301 imposition of other arbitrary high-order symmetries did not alter the radius of FliF's β-collar.
302 We conclude that the wider C-ring is achieved by *C. jejuni* assembling a wider MS-ring to
303 template the wider C-ring.

304 Discussion

305 This work provides a near-complete inventory of the proteins incorporated into the *C. jejuni*
306 motor during evolution of higher torque output, adaptations of pre-existing components (Fig.
307 6, Table S2), and insights into universal principles of flagellar rotation.

308 Our structures explain how the *C. jejuni* motor produces approximately three times the torque
309 of the *E. coli* and *Salmonella* motors. The spoke-and-rim scaffold of PflA and PflB, supported
310 by PflC and PlflD, positions stator complexes in a wider ring; these not only each exert greater
311 torque due to a greater lever length, but the torque from additional stator complexes is
312 additive[16,41]. This scaffold facilitates the high occupancy or static positioning of the *C. jejuni*
313 stator complexes[16]; the radius of the MS-ring is correspondingly larger than that of *Salmonella*
314 to template a wider C-ring to maintain contact with the larger stator ring. PflA and PflB are
315 composed of arrays of TPR motifs, widespread building blocks of structural scaffolds. The
316 widespread nature of TPR motifs would have made them available for co-option to form PflA
317 or PflB. Intriguingly, parts of the Tol/Pal system homologous to other flagellar proteins[6] and
318 the Tol/Pal component YbgF features TPR motifs[42], suggesting a scenario in which PflA and
319 PflB originated from another Tol/Pal co-option.

320 *C. jejuni*, the proximal disk is linked to the basal disk by the medial disk, while other species
321 lack a medial disk and have separate proximal and basal disks. Our structures provide insight
322 into the significance and mechanism of the relatively recent evolution of the medial disk[16]. We
323 recently showed that the basal disk has a distinct function in buttressing the motor when
324 unwrapping flagellar filaments from the cell body[20]. Here we identify PflC as the mediator of
325 the extensive connections between the proximal and basal disks[20] (Fig. 3, 4). PflC's shared
326 domain organisation and structure with HtrA-family enzymes suggests that it originated by co-
327 option of an HtrA family protein[43] (Extended Data Fig. 5A,C). Indeed, HtrA family proteins are
328 periplasmic, meaning that they already co-localised with the flagellar motor. Curiously, HtrA
329 also forms higher-order oligomers[29], suggesting that this oligomerisation tendency was a pre-
330 existing property easily exapted for its role as a structural scaffold. The proline-rich linker
331 between $PflC_N$ and $PflC_C$ is evidently important for the head-to-tail oligomerisation of PflC,
332 because species such as *Wolinella* and *Helicobacter,* which lack a medial disk, have PflC
333 sequences without this linker.

334 The basal disk is comparatively more ancient. While the basal disk protein FlgP comes from
335 a broad protein family, ring oligomerisation in the family correlates with the subset of
336 sequences that feature a β-hairpin insertion between the α-helix and second β-sheet, as seen
337 with the outer membrane-associated rings formed by FlgT, whose SHS2 domain features this
338 insertion[44]. Curiously, the basal disk from *Wolinella* has been proposed to form a spiral, not
339 concentric rings[45], raising the possibility that FlgP forms spirals in the absence of a medial
340 disk.

341 Our study sheds light on the universal mechanism of flagellar rotation. We discerned a
342 consistent rotational register of MotA, with vertices oriented toward the C-ring, and focused
343 classification of individual stator complexes failed to resolve classes with other rotational
344 registers. This is inconsistent with the homogenous circle predicted for averaged structures
345 given the continuum of rotational registers expected from a high duty ratio of the stator
346 complexes with FliG and the symmetry mismatch between the 17 stator complexes and 38-
347 fold symmetric C-ring. Predictions of stator complexes having a high duty ratio assumed an
348 elastic linker from peptidoglycan to MotA as in *Salmonella*[46], although this does not hold for
349 *C. jejuni* in which stator complexes are rigidly encased in their proteinaceous cage. Our
350 structure is therefore consistent with recent results suggesting that the stator complexes
351 having a low duty ratio[47], and MotA's rotational register is dictated by an energy minimum of
352 rotation around MotB instead of against FliG.

353 While our projection imaging approach achieves substantially higher resolution than previous
354 studies, enabling molecular interpretation and validation, our approach is not without

355 limitations. Our study focused on the 17-fold rotationally symmetric periplasmic scaffold, but
356 flagellar motors feature diverse symmetry-mismatched subcomponents. The approach can in
357 principle identify arbitrary symmetries, but we did not resolve symmetries for other
358 substructures such as the C-ring, likely due to weak signal due to their size, heterogeneity and
359 excessive noise from the *in situ* context. (Although useful information on these structures is
360 available from their cylindrical averages.) Different data acquisition schemes or mutants are
361 needed to understand how to extract this signal. Nevertheless, using minicells to study polar
362 machinery has promise for substantial increases in resolution in other systems, including Tad
363 pili[48] in *Caulobacter crescentus* minicells[49], type II secretion systems[50] in *Pseudomonas*
364 minicells[51], chemoreceptors in *C. jejuni*[52], and the flagellar motors of diverse other polar
365 flagellates[53,54].

366 Our approach achieved sufficient resolution of a bacterial molecular machine *in situ* for
367 molecular interpretation. Results provide invaluable information on the mechanisms of torque
368 generation and possible mechanisms of evolution, and will provide a foundation for further
369 comparative studies to probe how novel interfaces arose during protein recruitment. Our
370 approach confirms that imaging protein machines *in situ* can provide subnanometre resolution,
371 and lays a foundation for future studies expanding to other symmetry elements and structures.

372 Acknowledgements

373 We thank Paul Simpson in the Imperial College London Electron Microscopy Centre and the
374 Francis Crick Institute Structural Biology science technology platform for electron microscopy
375 assistance. This work was supported by Medical Research Council grant MR/V000799/1 to
376 EJC and MB, Human Frontier Science Program grant RGP0028/2021-HOCHBERG to MB
377 and GH, NIH grant R01AI065539 to DRH, BBSRC doctoral training grant BB/M011178/1 and
378 a short-term DAAD grant to TD. PBR is supported by the Francis Crick Institute, which receives
379 its core funding from Cancer Research UK (CC2106), the UK Medical Research Council
380 (CC2106), and the Wellcome Trust (CC2106). CMS is supported by research grants Sh580/7-
381 2 and Sh580/8-2 in the framework of the DFG (Deutsche Forschungsgemeinschaft) priority
382 program SPP2002 (Small proteins in prokaryotes, an unexplored world), the DFG Research
383 Training Group GRK2157 “3D-Infect”, and a “CampyRNA” junior consortium grant within the
384 2nd call of Infect-ERA (ERA-NET; www.infect-era.eu)/Bundesministerium für Bildung und
385 Forschung (BMBF; www.bmbf.de). ALN was supported by two French National Research
386 Agency (ANR) grants (PHY-BABIFO ANR-22-CE30-0034 and PHYBION ANR-23-ERCB-
387 0005-01). The CBS is a member of the France-BioImaging (FBI) and the French Infrastructure

for Integrated Structural Biology (FRISBI), two national infrastructures supported by the ANR (ANR-10-INBS-04-01 and ANR-10-INBS-05, respectively).

For the purpose of open access, the author has applied a Creative Commons Attribution (CC BY) license to any Author Accepted Manuscript version arising.

Author Contributions

TD: sample prep, image processing, analysis, molecular modelling, mass photometry, wrote paper; EJC: strain construction, sample prep, image processing, analysis; TC: image processing, manuscript and figure preparation; NS: image processing; TU: sample prep, data acquisition, image processing; AN: data acquisition, image processing; DR: flgQ-mCherry strain construction, pulldowns, fliL knockout; SS, KF, MA, CS: PflC and PflD identification; WHH, FP, ALN: experimental design, data acquisition, data analysis, funding acquisition; LDH: PflD subtomogram averaging; GH, SGG: Mass photometry data acquisition supervision and analysis, funding acquisition; DRH: strain construction, pulldowns, funding acquisition; PR: image processing, manuscript and figure preparation, funding acquisition; MB: conceptualization, funding acquisition, supervision, wrote paper

Declaration of Interests

The authors declare no competing interests.

Methods

Lead contact

Further information and requests for resources and reagents should be directed to and will be fulfilled by the lead contact, Morgan Beeby (mbeeby@imperial.ac.uk)

Materials availability

Plasmids and strains generated in this study (see Table S3) are available on request from the lead author.

Data and code availability

Cryo-EM maps have been deposited at the Electron Microscopy Data Bank (EMDB) and are publicly available as of the date of publication. The whole-motor map has been deposited with

415 accession code EMD-16723 together with the original micrographs deposited to the EMPIAR
416 repository with public accession code EMPIAR-11580 (DOI: 10.6019/EMPIAR-10016). The
417 refined periplasmic scaffold map has been deposited in the EMDB with accession code EMD-
418 16724. Subtomogram average maps were deposited as follows: Δ*pflC* - EMD-17415; Δ*pflD* -
419 EMD-17416; $pflA_{\Delta 16\text{-}168}$ - EMD-17417; FlgQ-mCherry - EMD-17419.

420 **Bacterial strains and culture conditions**

421 *C. jejuni* 81-176 or NCTC11168 were cultured from frozen stocks on Mueller-Hinton (MH) agar
422 (1.5% w/v) supplemented with trimethoprim (10 µg/mL) (MHT) for 1-2 days at 37 C under
423 microaerophilic conditions (5% O2, 10% CO2, 85% N2) in a in a Heracell 150i trigas incubator
424 (Thermo Fisher Scientific). Additional antibiotics were added to the agar medium when
425 required: kanamycin (Km) at 50 µg/mL, streptomycin (Sm) at 2 mg/mL. All 81-176 mutants
426 were constructed in DRH212[55], a streptomycin resistant derivative of *C. jejuni* 81-176, which
427 is the reference wild-type strain in this work unless otherwise stated. When working with *E.*
428 *coli*, cultures were grown at 37 C on Luria-Bertani (LB) agar plates (1.5% w/v) or in LB medium
429 with agitation, both supplemented with carbenicillin at 100 µg/ml. Please see Table S3 for
430 details of strains and plasmids used in this study.

431 ## *Method details*

432 **Strain construction**

433 The minicell (Δ*flhG* Δ*flaAB*) and PflA truncation ($pflA_{\Delta 18\text{-}168}$) strains were constructed as
434 described previously[55,56]. Briefly, *aphA-rpsL*^{WT} cassettes flanked by ~500 bp overhangs with
435 homology to the targeted chromosomal loci and ecoRI sites at the 5' and 3' termini were
436 synthesised by "splicing by overlap extension" PCR (SOE PCR). Linear DNA fragments were
437 methylated at their ecoRI sites with ecoRI methyltransferase (New England Biolabs) and
438 transformed into *C. jejuni* using the biphasic method[57]. Transformants were selected for on
439 MH agar supplemented with 50 µg/mL kanamycin. Replacement of the *aphA-rpsL*^{WT} with the
440 desired mutation was achieved using the same method, but with transformants being selected
441 for on MH agar supplemented with 2 mg/mL streptomycin sulfate. Kanamycin-sensitive,
442 streptomycin-resistant transformants were single-colony purified and checked by Sanger
443 sequencing (Source Biosciences UK). For the minicell background, in-frame deletion of *flhG*
444 leaves the first and last 20 codons intact, while the Δ*flaAB* allele spans from 20 base pairs
445 upstream of the *flaA* translational start site to codon 548 of *flaB*.

446 To construct the *C. jejuni fliL* mutant, we made a *cat* insertional knockout and confirmed
447 absence of polar effects. To preserve expression of the essential *acpS* gene downstream of

448 fliL, we constructed a *fliL* mutant that disrupted *fliL* with an antibiotic-resistance cassette
449 containing an intact flaA promoter positioned to maintain expression of acpS. First, the *fliL*
450 locus from *C. jejuni* 81-176 was PCR amplified with a HpaI site engineered within the *fliL*
451 coding sequence. This fragment was then cloned into the BamHI site of pUC19 to create
452 pDAR1712. The flaA promoter and start codon were PCR amplified from *C. jejuni* 81-176 and
453 cloned into the XbaI and BamHI sites of pUC19 to create pDAR2039. The chloramphenicol-
454 resistance cassette containing cat was digested as a PstI fragment from pRY109 and cloned
455 into PstI-digested pDAR2039 to create pDAR2045. The *cat-flaA* promoter was then digested
456 from pDAR2045 as a EcoRI-BamHI fragment, treated with T4 DNA polymerase to create blunt
457 ends and cloned into the HpaI site of pDAR1712 to create pDAR2072. pDAR2072 was verified
458 to contain the *cat-flaA* promoter in the correct orientation to maintain expression of *acpS*.
459 DRH212 was then electroporated with pDAR2072 and chloramphenicol-resistance
460 transformants were recovered. Colony PCR verified creation of a *fliL* mutant (DAR2076).

461 Deletion mutants of *C. jejuni* NCTC11168 were constructed by double-crossover homologous
462 recombination with an antibiotic resistance cassette to remove most of the coding sequence
463 using overlap PCR products. As an example, deletion of *cj1643* (*pflC*) is described. First, ~500
464 bp upstream of the *cj1643* start codon was amplified using CSO-3359/3360 and ~500 bp
465 downstream of the *cj1643* stop codon was amplified with CSO-3361/-3362 from genomic DNA
466 (gDNA) of the wild-type strain (CSS-0032). A non-polar kanamycin resistance cassette (*aphA-*
467 *3*, Kan^R) (Skouloubris et al., 1998) was amplified from pGG1[58] with primers HPK1/HPK2. To
468 fuse the up- and downstream regions of *cj1643* with the resistance cassette, the three
469 fragments were mixed and subjected to overlap-extension PCR with CSO-3359/ 3362. PCR
470 products were electroporated into the WT strain as previously described[59]. The final deletion
471 strain (CSS-4087; NCTC11168 Δ*cj1643*) was verified by colony PCR with CSO-3363/HPK2.
472 Deletion of *cj0892c* (*pflD*) in C. jejuni strain NCTC11168 was generated in a similar fashion:
473 *cj0892c*::*aphA-3* (CSS-4081; NCTC11168 Δ*cj0892c*).

474 To fuse *sfgfp* fusion to the penultimate codon of *cj0892c* (*pflD*), its coding sequence was first
475 amplified with CSO-3611/3612, digested with *Nse*I/*Cla*I, and inserted into similarly-digested
476 pSE59.1[60]; amplified with CSO-0347/CSO-0760) to generate pSSv106.5, where *cj0892c*
477 transcription is driven from the *metK* promoter. The plasmid was verified by colony PCR with
478 CSO-0644/3270 and sequencing with CSO-0759. Next, *sfgfp* was amplified from its second
479 codon from pXG10-SF[61] with CSO-3279/3717, digested with *Cla*I, and ligated to pSSv106.5
480 (amplified with CSO-3766/0347 and also digested with *Cla*I). This generated pSSv114.1,
481 which was verified by colony PCR with CSO-0644/0593 and sequencing with CSO-0759/3270.
482 The fusion of *rdxA*::P_{metK}-*cj0892c*-sfGFP was amplified from pSSv114.1 with CSO-2276/2277

483 and introduced into the *rdxA* locus of Δ*cj0892c* (CSS-4081) by electroporation. Clones were
484 verified via colony PCR and sequencing with CSO-0349 and CSO-0644. Colony PCR was also
485 used to confirm retention of the original deletion with CSO-3343 and HPK2.
486 Similar to construction of deletion mutants, C-terminal epitope tagged strains were generated
487 by homologous recombination at the native locus by electroporation of a DNA fragment. The
488 3xFLAG sequence was fused to the penultimate codon of the coding sequence to allow in-
489 frame translation of the tag. The DNA fragment contained ~ 500 bp upstream of the
490 penultimate codon of the gene of interest, the sequence of the epitope tag, a non-polar
491 resistance cassette, and the ~500 bp downstream sequence of the gene. As an example,
492 3xFLAG tagging of PflA (CSS-5714) is described. The upstream fragment was amplified with
493 CSO-4224 and CSO-4225 from *C. jejuni* NCTC11168 WT gDNA. The downstream fragment
494 was amplified using CSO-4226 and CSO-4227. The fusion of the 3xFLAG tag with the
495 gentamicin resistance cassette was amplified from *fliW*::3xFLAG-*aac*(3)-IV[58] using CSO-0065
496 and HPK2. Next, a three-fragment overlap PCR using CSO-4224 and CSO-4227 was
497 performed and the resulting PCR product was electroporated into CSS-4666. The obtained
498 clones were validated by PCR using CSO-4223 and HPK2 and by sequencing using CSO-
499 4223. PflB-3xFLAG (CSS-5716) and PflC-3xFLAG (CSS-4720) were generated similarly. The
500 3xFLAG with a non-polar kanamycin resistance cassette was amplified from *csrA*::3xFLAG-
501 *aphA*-3[58].

502 To construct a FlgQ-mcherry fusion protein for expression, a 76-bp DNA fragment containing
503 the cat promoter and start codon with an in-frame BamHI site from pRY109 was amplified by
504 PCR and cloned into the XbaI and XmaI sites of pRY112 to create pDAR1003. PCR was then
505 used to amplify mcherry from codon to the stop codon, which was then inserted into XmaI and
506 EcoRV sites of pDAR1003 to create pDAR1006. This plasmid contains a start codon that is
507 in-frame with DNA for BamHI and XmaI sites followed by the mcherry coding sequence.
508 Primers were then designed and used for PCR to amplify flgQ from codon 2 to the stop codon
509 from C. jejuni 81-176. This fragment was inserted in-frame into the BamHI site of pDARH1006
510 to create pDRH7476, which was then conjugated into DRH2071 to result in DRH7516.

511 **CryoEM sample preparation**

512 *C. jejuni* Δ*flhG* Δ*flaAB* cells were grown on MH plates and resuspended in phosphate-buffered
513 saline (PBS buffer, 137 mM NaCl, 2.7 mM KCl, 10 mM Na2HPO4, 1.8 mM KH2PO4, pH 7.4).
514 Cells were spun at 4,000 rpm for 20 min to pellet whole cells. The minicell-enriched
515 supernatant was removed and spun in a tabletop microcentrifuge at 15,000 rpm for 5 min to
516 pellet the minicells. The pellet was then resuspended to a theoretical OD600 of ~15.

517 Minicells were vitrified on QUANTIFOIL® R0.6/1 or R1.2/1.3 holey carbon grids (Quantifoil
518 Micro Tools) using a Vitrobot Mark IV (Thermo Fisher Scientific).

519 For cryoET, whole-cells were grown on MHT agar, re-streaked on fresh plates and grown
520 overnight before use. Freshly grown cells were suspended into ~1.5 mL of PBS buffer and
521 concentrated to an approximate theoretical OD_{600} of 10 by pelleting at 3000 rpm for 5 min on
522 a tabletop microcentrifuge and resuspending appropriately. 30 µL of the concentrated cell
523 sample was mixed with 10 nm gold fiducial beads coated with bovine serum albumin (BSA).
524 3 µL of this mixture was applied to freshly glow-discharged QUANTIFOIL® R2/2, 300 mesh
525 grids. Grids were plunge-frozen in liquified ethane-propane using a Vitrobot mark IV.

526 **Single particle analysis image acquisition**

527 Micrographs of the minicell sample were collected using 300 keV Thermo Fisher Scientific
528 Titan Krios TEMs, across two sessions using EPU acquisition software. The first dataset was
529 collected on a microscope with a Falcon III direct electron detector (Thermo Fisher Scientific),
530 the second dataset using a K2 direct electron detector equipped with a GIF energy filter
531 (Gatan), using a slit width of 20 eV. Due to our large particle size relative to that of the holes,
532 we collected one shot per hole. Gain correction was performed on-the-fly. Details of data
533 collection parameters are described in Table 1.

534 **Tilt series acquisition**

535 Tilt series of motors in *pflA*$_{\Delta 18\text{-}168}$ were collected using a 300 keV Titan Krios TEM (Thermo
536 Fisher Scientific) equipped with a K2 direct electron detector and a GIF energy filter (Gatan)
537 using a slit width of 20 eV. Data was collected in Tomography 5 (Thermo Fisher Scientific)
538 using a dose-symmetric tilt scheme across ±57° in 3° increments. We used a dose of 3 e-/Å^2
539 per tilt, distributed across 4 movie frames. The pixel size was 2.2 Å and defocus range from -
540 4.0 to -5.0 µm. To determine the *C. jejuni* C-ring architecture, tilt series of 194 motors in
541 DRH8754 were collected using a 200 keV Glacios TEM (Thermo Fisher Scientific) equipped
542 with a Falcon 4 direct electron detector and a Selectris energy filter (Thermo Fisher Scientific)
543 using a slit width of 10 eV. Data was collected in Leginon automated data-collection software
544 using a dose-symmetric tilt scheme across ±51° in 3° increments. We used a dose of 2.7 e-
545 /Å^2 per tilt, distributed across 5 movie frames. The pixel size was 1.9 Å and defocus was -4.0
546 µm. All other tilt series datasets were acquired on a 200 keV FEI Tecnai TF20 FEG
547 transmission electron microscope (FEI Company) equipped with a Falcon II direct electron
548 detector camera (FEI Company) using Gatan 914 or 626 cryo-holders. Tilt series were
549 recorded from −57° to +57° with an increment of 3° collected defocus of approximately −4 µm

using Leginon automated data-collection software at a nominal magnification of 25,000× and were binned two times. Cumulative doses of ∼120 e−/Å2 were used. Overnight data collection was facilitated by the addition of a 3-L cold-trap Dewar flask and automated refilling of the Dewar cryo-holder triggered by a custom-written Leginon node interfaced with a computer controlled liquid nitrogen pump (Norhof LN2 Systems).

Single particle analysis

Movie frames were aligned and dose-weighted according to exposure, as implemented in MotionCor2 version 2.1[62]. All subsequent processing was done in RELION 3.1[63,64]. CTF-correction was performed using CTFFIND4[65], using the RELION wrapper. Flagellar motor positions were picked manually, yielding 79,287 particle coordinates for the K2 dataset and 14,605 particle coordinates in the F3 dataset.

The two datasets were first processed separately in RELION 3.1, before merging for a final round of refinement For the K2 dataset, 79287 particles were extracted at a box size of 800 px. A round of 2D classification removed junk and membrane particles, and an initial model was created using these particles with imposed C17 symmetry, which is known from past structural characterisation of the motor by subtomogram averaging[16]. A round of mask-free 3D classification and refinement with applied C17 symmetry produced the first consensus refinement. 27,164 particles were then re-extracted, centering on the periplasmic structures. After another round of 3D classification, 19,736 particles were refined in C17 symmetry to produce a whole-motor reconstruction at 9.88 Å using gold-standard refinement. For the F3 data, 14,605 particles were extracted at a box size of 1000 px rescaled to 500 px. They underwent 2D classification to remove junk, 3D classification and refinement to arrive at an initial consensus 3D structure. The particles were again re-centered on the periplasmic structures and underwent another round of refinement. Finally, the 13,054 particles were re-extracted at an un-binned 1000 px box size for a final round of refinement. The two re-centered refined datasets were merged, assigning them different RELION 3.1 optics groups, and refined to a global resolution of 9.36 Å (32,790 total particles).

Signal subtraction was used to further refine the structure of the periplasmic scaffold. A mask encompassing the regions of interest was made by segmenting and smoothing the whole-motor map using UCSF Chimera 1.16[66,67] and its Segger plugin[68], binarising and adding a soft-edge in RELION 3.1. The mask included the periplasmic scaffold and first ring of the basal disk, as the scaffold appears to attach onto it. This mask was used to computationally remove signal outside of the periplasmic regions of interest, as implemented in RELION 3.1. The signal subtraction and subsequent masked classification and refinement was conducted for the

584 combined dataset, as well as K2 and F3 datasets separately. The highest resolution was
585 reached with the merged data, the periplasmic scaffold map reaching 7.68 Å from 32,790
586 particles.

587 The periplasmic scaffold map was post-processed using LAFTER[69] as implemented in the
588 CCP-EM 1.6.0 software suite[70] to suppress noise and enhance signal between the half-maps.
589 The LAFTER-filtered map of the scaffold was used for docking and modelling of periplasmic
590 regions.

591 **Focused refinement of LP-, MS- and C-rings**

592 After convergence of the full-motor refinement in C17 symmetry, focused refinement of the
593 MS- LP- and C-rings was carried out, using a lathed map lacking azimuthal features. C17 map
594 was lathed by applying C360 symmetry using EMAN2, producing a map with axial and radial
595 features but no azimuthal features. This map was used as a reference for asymmetric
596 refinement, so that no bias towards a particular cyclic symmetry could be imposed.

597 For the LP-ring, a tubular mask covering the LP-ring was used for signal subtraction and
598 focused refinement. Subtracted particles were recentred on the LP-ring in a smaller 256-pixel
599 box. A recentred subvolume of the full lathed map was used for the initial reference.
600 Refinement with imposition of C26 symmetry produced the LP-ring localised reconstruction.

601 For the MS-ring, a tubular mask covering the MS-ring was used for signal subtraction and
602 focused refinement. Subtracted particles were recentred on the MS-ring in a smaller 256-pixel
603 box. A recentred subvolume of the full lathed map was used for the initial reference.
604 Refinement with imposition of C38 symmetry produced the MS-ring localised reconstruction.

605 For the C-ring, a toroidal mask covering the C-ring was used for signal subtraction and focused
606 refinement against the full-size lathed motor map. Refinement with imposition of C38
607 symmetry produced the C-ring localised reconstruction. This map was then postprocessed
608 and sharpened with an empirically determined B factor of -1200 $Å^2$.

609 **Focused classification of stator complexes**

610 From the full-motor refinement in C17 symmetry, particles were symmetry expanded and re-
611 windowed into a smaller 360-pixel box centred on a stator complex, with subtraction of the
612 surrounding signal using a spherical mask encompassing a triplet of neighbouring stator
613 complexes. Classification without alignment produced the stator maps shown.

614 **Subtomogram averaging**

615 Fiducial models were generated and tilt series were aligned for tomogram reconstruction using
616 the IMOD package[71]. Tomo3D[72] was used to reconstruct tomograms with the SIRT method
617 due to approximately 1 particle per tomogram. All steps were automated by in-house custom
618 scripts.

619 Subtomogram averaging was performed using the Dynamo package[73] unless otherwise
620 stated. Motors were picked using 3dmod from the IMOD suite and imported into Dynamo as
621 'oriented particles' using an in-house script, and subtomograms were extracted for averaging.
622 For each structure, an initial model was obtained by reference-free averaging of the oriented
623 particles, with randomized Z-axis rotation to alleviate missing wedge artefacts. This initial
624 model was used for a first round of alignment and averaging steps, implementing an angular
625 search and translational shifts, with cone diameter and shift limits becoming more stringent
626 across iterations. The resulting average was used as a starting model for a round of masked
627 alignment and averaging. In this round, custom alignment masks were implemented, focusing
628 on the periplasmic and inner membrane-associated parts of the motor. This excluded
629 dominant features that would otherwise drive the alignment, most prominently the outer
630 membrane and extracellular hook. 17-fold rotational averaging was applied. The final *pflA*$_{\Delta 18-}$
631 $_{168}$ average was derived from 103 particles. The Δ*pflC* average from 101 particles, Δ*pflD*
632 average from 195 particles, and the *flgQ-mCherry* average from 155 particles.

633 The *C. jejuni* C-ring subtomogram average using DRH8754 used the PEET package[74].
634 Tomograms were CTF corrected using IMOD, motors picked using 3dmod, and
635 subtomograms extracted for averaging in PEET. After an initial C1 whole-motor alignment, a
636 subsequent alignment recentred on the tightly-masked C-ring was performed. To capitalise on
637 the redundancy of C-ring archecture and to increase the number of particles, each motor was
638 then symmetry expanded so that the C-ring beneath each of the 17 asymmetric units could be
639 treated as a separate particle. Subsequent alignment and classification to remove poorly-
640 aligned particles yielded the final structure.

641 **De novo Modelling**

642 ColabFold[75], the community-run implementation of Deepmind's AlphaFold2[26] was used to
643 create structural models of PflA, PflB, a dimer of PflA-PflB, PflC, PflD, FlgP (as a monomer,
644 trimer, and heptamer), FlgQ, FliL, and a dimer of $MotB_C$ (with transmembrane residues 1-67
645 removed).

646 The PflAB dimer model was created by merging two predicted structures - that of a dimer of
647 PflA residues 16-455 and PflB residues 113-820, and full-length PflA.

648 **Docking and refinement**

649 For regions where α-helices and β-sheets were resolved, we refined our AlphaFold predicted
650 protein models into the scaffold map using ISOLDE[76] in UCSF Chimera X 1.6. We imposed
651 torsion, secondary structure, and reference distance restraints in our modelling due to
652 resolution limitations. The PflB chain of the PflAB dimer was rigidly docked into the map, the
653 PflA chain was refined into the appropriate density, and any clashes resolved. Models of FlgP
654 multimers showed that each subunit interacts with subunits i−1 and i−2. To avoid artefacts
655 due to this, a heptamer of FlgP was docked into the innermost basal disk ring and then refined
656 into the map. Two subunits were then removed from each end, resulting in a fitted FlgP trimer.
657 The PflC model was first separated into three domains, $PflC_N$ (residues 16-252), linker (253-
658 263), and $PflC_C$ (264-364). Each domain was rigidly docked into its appropriate density, the
659 three chains merged, and the resulting protein was fitted using ISOLDE to resolve clashes or
660 poor geometry at merging points. Six copies of $PflC_N$ were rigidly docked into an asymmetric
661 unit of PflC lattice in the medial disk, forming $PflC_{2\text{-}7}$. PflD, MotB, and an arc of FliL, were rigidly
662 docked into the LAFTER-filtered scaffold map.

663 We used *phenix.validation_cryoem* from the Phenix package[77] to evaluate map and model
664 quality for PflA, PflB, PflC, $PflC_{2\text{-}7}$, PflD, FlgP trimer, MotB dimer, and FliL. For each model, a
665 soft mask of the region was first created and applied to the map. The resulting masked volume
666 and corresponding structural model were input to *phenix.validation_cryoem* which generated
667 map-model FSC plots or cross-correlation scores.

668 **Flagellar motility assays**

669 WT *C. jejuni* and DAR2076 were grown from freezer stocks on MH agar containing
670 trimethoprim for 48 h in microaerobic conditions at 37 C. Strains were restreaked on MH agar
671 containing trimethoprim and grown for 16 h at 37 C in microaerobic conditions. After growth,
672 strains were resuspended from plates and diluted to an OD_{600} 0.8. Strains were then stabbed
673 in MH motility agar (0.4% agar) and incubated at 37 C in microaerobic conditions for 30 h and
674 assessed for migration from the point of inoculation.
675

676 **Bead assay of rotational steps**

677 The *C. jejuni* bead assay strain was constructed by deleting *flaA* to shorten the flagellar
678 filament, making a cysteine substitution in *flaB* to allow for filament bi- otinylation via a

679 malemide-PEG2-biotin linker (Thermo Scientific A39261), making an alanine substitution in
680 *flhF* which moves motors to a subpolar position permitting better bead coupling, and deleting
681 *cheY* to prevent motor switching. From frozen stocks, this strain was cultured on Mueller-
682 Hinton agar (1.4% w/v) supplemented with trimethoprim (10 μg/mL) overnight at 37 ◦C in a
683 pouch with a gas-controlling sachet (EZ CampyPouch System BD 260685) and a damp paper
684 towel. The growth from this culture was restreaked onto another plate and grown in the same
685 conditions overnight. Passages to new plates on the following two days were optionally made
686 to propagate the culture for multiple days of experiments.

687 After growth, bacteria were washed off the plate with MH broth and washed twice with PBS
688 (centrifuged for 2 min at 11 500 RPM) to create a 500 μL suspension of OD_{600} of 2. Next, 25
689 μL of 20 mM malemide-PEG2-biotin linker in PBS was added and left to react for 10 min. The
690 bacteria were then washed twice more in PBS. A custom tunnel slide composed of a slide with
691 two drilled holes, a parafilm spacer, and another glass slide was constructed and connected
692 to a peristaltic pump (Lambda Multiflow) to draw flow through the slide. Poly-L-lysine (PLL)
693 solution (Sigma-Aldrich P4707) was flowed into the slide channel and left for 5 min to coat the
694 glass surface. Excess PLL was flushed with PBS. Bacteria were added and left 5 min to settle
695 on the surface. Unattached bacteria were flushed sequentially with PBS and MH broth. 1300
696 nm diameter, streptavidin-coated beads (Sigma-Aldrich 49532) were washed once in PBS and
697 dispersed in MH broth. Beads were added to the flow slide and left for 5 min to settle and
698 conjugate to filaments. Excess beads were flushed away with MH-broth. Spinning beads were
699 observed with a bright-field microscope with a high numerical aperture (NA) objective (100×,
700 1.46 NA, Zeiss 420792-9800-720) and recorded with a high speed scientific complementary
701 metal-oxide semiconductor camera (Optronis CL600X2-FULL-M-FM). Positions of slowly-
702 rotating beads attached to cells treated with carbonyl cyanide 3-chlorophenylhydrazone
703 (CCCP) at concentrations of 0 μM to 5 μM in MH broth revealed preferred phase-invariant
704 dwell positions.

705 **Plasmid construction and cloning in E. coli**

706 *C. jejuni* proteins for recombinant expression in *E. coli* were cloned into the pLIC plasmid
707 backbone, which confers resistance to ampicillin and places the gene of interest under an
708 IPTG-inducible T7 promoter for high levels of controlled expression. We used WT *C. jejuni*
709 genomic DNA as template for gene amplification (extracted using the Wizard genomic DNA
710 purification kit by Promega), and the Gibson Assembly method[78] to seamlessly assemble all
711 plasmid constructs. For all constructs, primer pairs were designed to amplify 1) the pLIC
712 backbone and 2) the gene to be expressed, while also introducing a 25~30 bp complementary
713 overlap between the two fragments. The pLIC plasmid primers also introduced an N-terminal

714 hexahistidine tag. After vector linearisation and purification of PCR product, it was digested
715 with DpnI (New England Biolabs) to remove template vector.

716 The resulting linear DNA fragments were assembled using the Gibson Assembly master mix
717 (New England Biolabs). 5 µL of mix was added to 15-20 fmol of linearised vector and 4×
718 excess of insert and topped up to 10 µL with double-distilled water (ddH_2O). The tube was
719 incubated at 50 C for 15 min and kept on ice until transformation.

720 Before transformation, 30 µL of ddH_2O was added to the 10 µL reaction. 2 µL of diluted Gibson
721 mix was added to 25 µL of chemically competent *E. coli* DH5α and transformed using the heat
722 shock method[79]. The entire volume of the tube was then plated onto a carbenicillin-
723 supplemented LB agar plate.

724 After confirmation by Sanger sequencing (Source Bioscience), each assembled construct was
725 isolated from the cloning strain (QIAprep Spin Miniprep Kit, QIAGEN) and transformed into E.
726 coli BL21(DE3) for recombinant overexpression.

727 **Protein overexpression and purification**

728 All proteins encoded on pLIC expression vectors were purified using the same protocol. A
729 small (5 mL) overnight liquid culture of *E. coli* BL21(DE3) carrying the appropriate expression
730 vector was prepared and diluted 1:50 in 1000 mL of LB medium. Shaking at 37 C, the culture
731 was grown to OD600 0.4-0.6, after which protein expression was induced by addition of 0.5
732 mM IPTG. Temperature was reduced to 18 C and protein was expressed overnight.

733 Cells were harvested at 5000 rpm, 4 C for 20 min. All subsequent steps were done on ice
734 using buffers chilled to 4 C. The cell pellet was gently resuspended in ~35 mL of wash buffer
735 (50 mM Tris-HCl, 100 mM NaCl, 30 mM imidazole, pH 7.5). DNase and protease inhibitor
736 were added (cOmplete Protease Inhibitor Cocktail, Roche). Cells were lysed using a LM10
737 Microfluidizer Processor cell disrupter (Analytik) at 15,000 psi. Lysate was centrifuged at
738 17,000 rpm, 4 C for 30 min to pellet debris. The resulting supernatant was filtered through a
739 0.45 µm syringe filter (Whatman).

740 A 5 mL HisTrap HP affinity chromatography nickel column (Cytiva) was first equilibrated with
741 wash buffer. Supernatant was loaded onto the column with a peristaltic pump at a flow rate of
742 3 mL/min. The column was washed with 50 mL of wash buffer and then transferred onto a
743 Fast protein liquid chromatography system (BioRad). The column was further washed until the
744 UV trace was flat. Then, protein was eluted from the column using a high-imidazole buffer (50
745 mM Tris-HCl, 100 mM NaCl, 500 mM imidazole, pH 7.5) at a flow of 2 mL/min using 'reverse
746 flow'.

747 The purified protein was kept at 4 C or flash-frozen in LN2 for longer-term storage before
748 characterising them by mass photometry.

749 **Analytical size exclusion**

750 Analytical size exclusion of PflC and $PflC_N$ (Δ236-349) was performed with a ENrich SEC 650
751 column (Bio-Rad), equilibrated with 1× PBS at a flow rate of 0.1 ml min−1 and a total sample
752 injection volume of 400 µl. The column was calibrated using the Protein Standard Mix 15 –
753 600 kDa (Supelco #69385). Absorption was recorded at 280, 220 and 495 nm to follow elution
754 profiles and plotted using GraphPad Prism.

755 **Protein pulldowns**

756 **Co-immunoprecipitation (coIP) of PflA/B-3xFLAG with PflD-sfGFP, and PflC-3xFLAG**
757 Chromosomally epitope-tagged fusions of PflC-3xFLAG (CSS-4720) or PflA-3xFLAG and
758 PflD-sfGFP (CSS-5714), and PflB-3xFLAG and PflD-sfGFP (CSS-5716) were used together
759 with the untagged *C. jejuni* NCTC11168 WT (CSS-0032) and PflD-sfGFP only (CSS-4666) as
760 controls for immunoprecipitation. Co-purification of FlgP or PflD-sfGFP was investigated by
761 western blot (WB) analysis using FlgP specific antisera[19] or an anti-GFP antibody (Roche
762 #11814460001, RRID:AB_390913), respectively. In brief, strains were grown to an OD_{600} of
763 0.6 and 60 OD_{600} of cells were harvested (5,000 rpm, 20 min, 4 C) and washed in buffer A
764 (20 mM Tris-HCl pH 8, 1 mM $MgCl_2$, 150 mM KCl, 1 mM DTT). In parallel, 1 OD_{600} of cells was
765 harvested as "culture" control and boiled in 1 x protein loading buffer (PL; 62.5 mM Tris-HCl,
766 pH 6.8, 100 mM DTT, 10% (v/v) glycerol, 2% (w/v) SDS, 0.01% (w/v) bromophenol blue; 8
767 min at 95 C, shaking at 1,000 rpm). Next, 60 OD_{600} cell pellets were lysed with a FastPrep
768 system (MP Biomedical, matrix B, 1 x 4 m/s, 10 s) in 1 ml lysis buffer [buffer A including 1 mM
769 PMSF (phenylmethylsulfonyl fluoride, Roche), 20 U DNase I (Thermo Fisher Scientific), 200
770 U RNase Inhibitor (moloX, Berlin) and Triton X-100 (2 µl/ml lysis buffer)]. Cleared lysates
771 (13,000 rpm, 10 min, 4 C) were incubated with 35 µl anti-FLAG antibody (Sigma-Aldrich,
772 #F1804-1MG, RRID:AB_262044) for 30 min at 4 C with rotation. Before and after incubation,
773 a 1 OD_{600} aliquot was taken aside as lysate and supernatant 1 samples. Lysates with anti-
774 FLAG antibody were then incubated for additional 30 min (4 C, rotating) with 75 µl/sample pre-
775 washed (3 times in buffer A) Protein A-Sepharose beads (Sigma-Aldrich, #P6649). Afterwards,
776 the supernatant/unbound fraction was removed after centrifugation (15,000 x g, 1 min, 4 C;
777 supernatant 2) and Protein A-Sepharose beads with bound proteins were washed 5 times with
778 buffer A. Elution of the bound proteins was performed with boiling of the beads in 400 µl 1 x
779 PL (8 min at 95 C, 1,000 rpm). Six volumes of acetone were used to precipitate eluted proteins
780 overnight at -20 C. Next, precipitated proteins were harvested by centrifugation (15,000 rpm,

781 1 h, 4 C), air-dried and resuspended in 1 x PL. Culture, lysate, supernatants 1 & 2, wash
782 (aliquots corresponding to 0.1 OD_{600}) and eluate samples (corresponding to 10 OD_{600}) were
783 analysed by WB. Western Blots were performed as described previously[58] and probed with
784 the appropriate primary antibodies (anti-FLAG, anti-GFP (1:1,000 in 3% BSA/TBS-T)) or FlgP
785 antisera (1:20,000 in 3% BSA/TBS-T) and secondary antibodies (anti-mouse or anti-rabbit
786 IgG, HRP-conjugate (1:10,000) in 3% BSA/TBS-T; GE Healthcare, #RPN4201 and
787 #RPN4301, respectively).

788 **Mass Photometry**

789 Microscope coverslips (24 × 60 mm, Carl Roth) and CultureWell Gaskets (CW- 50R-1.0, 50-3
790 mm diameter × 1 mm depth) were cleaned with alternating ddH_2O and 100% isopropanol
791 washes, then dried roughly with pressurised air and left to dry further overnight at room
792 temperature. Before use, gaskets were assembled onto coverslips and placed on the lens of
793 a One^{MP} mass photometer (Refeyn Ltd) with immersion oil.

794 For each measurement, a gasket was first filled with 18 µL of PBS buffer and the instrument
795 was focused. Then, 2 µL of sample was added to the droplet and rapidly mixed by pipetting.
796 Measurements were then started using AcquireMP v1.2.1 (Refeyn Ltd). For each
797 measurement, data was acquired for 60 s at 100 frames per second. Mass photometry data
798 was processed and analyzed in DiscoverMP software v.1.2.3 (Refeyn Ltd).

799 Measurements were conducted using affinity chromatography-purified proteins diluted to 200-
800 800 nM, calculated from absorption at 280 nm. 2 µL of sample was added to 18 µL PBS droplet
801 and mixed. For measurements of hetero-oligomers, the different proteins were first combined
802 and mixed in a separate tube and subsequently applied to the PBS droplet. MP measurements
803 were calibrated against molecular masses of commercial NativeMark^{TM} unstained protein
804 standard (Thermo Fisher Scientific). 1 µL of NativeMark^{TM} was diluted 30-fold in PBS and 2
805 µL of this solution was added to 18 µL PBS for measurement. Detected peaks corresponded
806 to 66 kDa, 146 kDa, 480 kDa, and 1048 kDa and were used to calibrate subsequent
807 measurements in DiscoverMP.

808 **Construction of plasmids and strains for PflA and PlfB co-immunoprecipitation**
809 **experiments**

810 Plasmids were constructed with specific promoters for expression of FLAG-tagged proteins in
811 *C. jejuni* mutants for co-immunoprecipitation experiments. To express a C-terminal FLAG-
812 tagged PflA protein, a 206-base pair DNA fragment from *C. jejuni* 81-176 that contained the
813 promoter for *flaA* encoding the major flagellin with its start codon and an in-frame SpeI
814 restriction site followed by an in-frame BamHI restriction site was amplified by PCR. This

815 fragment was cloned into the XbaI and BamHI sites of pRY108 to result in pDAR1425. Primers
816 were then constructed to amplify DNA from codon 2 to the penultimate codon of *pflA* from *C.*
817 *jejuni* 81-176 with an in-frame C-terminal FLAG tag epitope and stop codon. This DNA
818 fragment was then cloned into the BamHI site of pDAR1425 so that *pflA*-FLAG was expressed
819 from the flaA promoter to create pDAR3417. As a control, a 229-base pair DNA fragment from
820 *C. jejuni* 81-176 that contained the promoter for *flaA* encoding the major flagellin with its start
821 codon and DNA encoding an in-frame FLAG tag epitope followed by an in-frame BamHI
822 restriction site was cloned into the XbaI and BamHI sites of pRY108 to create pDAR1604.
823 pDAR1604 and pDAR3417 were then moved into DH5a/pRK212.1 for conjugation into
824 DAR1124. Transconjugants were selected for on media with kanamycin and verified to contain
825 the correct plasmids to result in DAR3447 and DAR3477.

826 To express a C-terminal FLAG-tagged PflB protein, primers were constructed to amplify DNA
827 from codon 2 to the penultimate codon of pflB from *C. jejuni* 81-176 with an in-frame C-terminal
828 FLAG tag epitope and stop codon. This DNA fragment was then cloned into the BamHI site of
829 pECO102 so that pflB-FLAG was expressed from the cat promoter to create pDAR3414.
830 pDAR965 and pDAR3414 were then moved into DH5a/pRK212.1 for conjugation into
831 DAR981. Transconjugants were selected for on media containing chloramphenicol and
832 verified to contain the correct plasmids to result in DAR3451 and DAR3479.

833 **PflA and PflB co-immunoprecipitation experiments**

834 *C. jejuni* Δ*pflA* and Δ*pflB* mutants containing plasmids to express a FLAG-tag alone or C-
835 terminal FLAG-tagged PflA or PflB proteins were grown from freezer stocks on MH agar
836 containing chloramphenicol for 48 h in microaerobic conditions at 37 C. Each strain was
837 restreaked onto two MH agar plates containing chloramphenicol and grown for 16 h at 37 C
838 in microaerobic conditions. After growth, strains were resuspended from plates in PBS and
839 centrifuged for 10 min at 6000 rpm. Each cell pellet was resuspended in 2 ml of PBS.
840 Formaldehyde was added to a final concentration of 0.1% and suspensions were gently mixed
841 for 30 min at room temperature to crosslink proteins. After crosslinking, 0.4 ml of 1 M glycine
842 was added to each sample and then suspensions were gently mixed for 10 min at room
843 temperature to quench the crosslinking reaction. Bacterial cells were collected by
844 centrifugation for 10 min at 6000 rpm. Cells were then disrupted by osmotic lysis and FLAG-
845 tagged proteins with associated interacting proteins were immunoprecipitated with α-FLAG
846 M2 affinity resin as previously described[80,81].

847 To identify potential proteins interacting with PflA and PflB, resin with immunoprecipitated
848 proteins were resuspended in SDS-loading buffer and electrophoresed on a 4-20% TGX stain-
849 free gel (Bio-Rad) for 10 min. The gel was then stained with Coomassie blue for 30 min and

850 then destained overnight. After equilibration of the gel in dH_2O for 30 min, a 1 cm region of the
851 gel containing a majority of the co-immunoprecipitated proteins was excised and diced into 1
852 mm pieces and then submitted for analysis by LC-MS/MS. After identification of proteins that
853 co-immunoprecipitated with the FLAG-tagged bait protein and with the resin from the FLAG-
854 tag only sample (the negative control), a ratio for each protein was determined by dividing the
855 abundance of each protein detected in the FLAG-tagged bait protein sample by the abundance
856 of each protein in the negative control. The top twenty proteins with the highest ratios for co-
857 immunoprecipitation with the FLAG-tagged bait proteins are reported. The top twenty proteins
858 that only co-immunoprecipitated with the FLAG-tagged bait proteins and were not detected in
859 the negative control samples are also reports with their respective raw abundance counts.

860 References

861 1. Johnson, A. D. The rewiring of transcription circuits in evolution. *Current Opinion in*
862 *Genetics & Development* **47**, 121–127 (2017).
863 2. Bridgham, J. T., Carroll, S. M. & Thornton, J. W. Evolution of hormone-receptor complexity
864 by molecular exploitation. *Science* **312**, 97–101 (2006).
865 3. Finnigan, G. C., Hanson-Smith, V., Stevens, T. H. & Thornton, J. W. Evolution of increased
866 complexity in a molecular machine. *Nature* **481**, 360–364 (2012).
867 4. Pillai, A. S. *et al.* Origin of complexity in haemoglobin evolution. *Nature* **581**, 480–485
868 (2020).
869 5. Schulz, L. *et al.* Evolution of increased complexity and specificity at the dawn of form I
870 Rubiscos. *Science* **378**, 155–160 (2022).
871 6. Beeby, M., Ferreira, J. L., Tripp, P., Albers, S.-V. & Mitchell, D. R. Propulsive
872 nanomachines: the convergent evolution of archaella, flagella and cilia. *FEMS Microbiol*
873 *Rev* **44**, 253–304 (2020).
874 7. Singh, P. K. *et al.* CryoEM structures reveal how the bacterial flagellum rotates and
875 switches direction. *Nat Microbiol* 1–11 (2024) doi:10.1038/s41564-024-01674-1.
876 8. Johnson, S. *et al.* Structural basis of directional switching by the bacterial flagellum. *Nat*
877 *Microbiol* 1–11 (2024) doi:10.1038/s41564-024-01630-z.

878 9. Deme, J. C. *et al.* Structures of the stator complex that drives rotation of the bacterial
879 flagellum. *Nat Microbiol* **5**, 1553–1564 (2020).
880 10. Santiveri, M. *et al.* Structure and Function of Stator Units of the Bacterial Flagellar Motor.
881 *Cell* **183**, 244-257.e16 (2020).
882 11. Johnson, S. *et al.* Molecular structure of the intact bacterial flagellar basal body. *Nat*
883 *Microbiol* **6**, 712–721 (2021).
884 12. Tan, J. *et al.* Structural basis of assembly and torque transmission of the bacterial flagellar
885 motor. *Cell* **184**, 2665-2679.e19 (2021).
886 13. Shibata, S., Matsunami, H., Aizawa, S.-I. & Wolf, M. Torque transmission mechanism of
887 the curved bacterial flagellar hook revealed by cryo-EM. *Nat Struct Mol Biol* 1–5 (2019)
888 doi:10.1038/s41594-019-0301-3.
889 14. Kreutzberger, M. A. B. *et al.* Convergent evolution in the supercoiling of prokaryotic
890 flagellar filaments. *Cell* **185**, 3487-3500.e14 (2022).
891 15. Terashima, H., Fukuoka, H., Yakushi, T., Kojima, S. & Homma, M. The Vibrio motor
892 proteins, MotX and MotY, are associated with the basal body of Na+-driven flagella and
893 required for stator formation. *Molecular Microbiology* **62**, 1170–1180 (2006).
894 16. Beeby, M. *et al.* Diverse high-torque bacterial flagellar motors assemble wider stator rings
895 using a conserved protein scaffold. *PNAS* 201518952 (2016)
896 doi:10.1073/pnas.1518952113.
897 17. Chaban, B., Coleman, I. & Beeby, M. Evolution of higher torque in Campylobacter- type
898 bacterial flagellar motors. *Scientific Reports* **8**, 97 (2018).
899 18. Beeby, M. Motility in the epsilon-proteobacteria. *Current Opinion in Microbiology* **28**, 115–
900 121 (2015).
901 19. Sommerlad, S. M. & Hendrixson, D. R. Analysis of the roles of FlgP and FlgQ in flagellar
902 motility of Campylobacter jejuni. *J. Bacteriol* **189**, 179–186 (2007).

903 20. Cohen, E. J. *et al.* Evolution of a large periplasmic disk in Campylobacterota flagella
904 facilitated efficient motility alongside autoagglutination. 2023.09.08.556628 Preprint at
905 https://doi.org/10.1101/2023.09.08.556628 (2023).
906 21. Chang, Y. *et al.* Molecular mechanism for rotational switching of the bacterial flagellar
907 motor. *Nat Struct Mol Biol* **27**, 1041–1047 (2020).
908 22. Liu, Y. & Sigworth, F. J. Automatic cryo-EM particle selection for membrane proteins in
909 spherical liposomes. *Journal of Structural Biology* **185**, 295–302 (2014).
910 23. Tonggu, L. & Wang, L. Structure of the Human BK Ion Channel in Lipid Environment.
911 *Membranes* **12**, 758 (2022).
912 24. Balaban, M. & Hendrixson, D. R. Polar Flagellar Biosynthesis and a Regulator of Flagellar
913 Number Influence Spatial Parameters of Cell Division in Campylobacter jejuni. *PLoS*
914 *Pathog.* **7**, e1002420 (2011).
915 25. Butan, C., Lara-Tejero, M., Li, W., Liu, J. & Galán, J. E. High-resolution view of the type III
916 secretion export apparatus in situ reveals membrane remodeling and a secretion pathway.
917 *Proceedings of the National Academy of Sciences* **116**, 24786–24795 (2019).
918 26. Jumper, J. *et al.* Highly accurate protein structure prediction with AlphaFold. *Nature* 1–11
919 (2021) doi:10.1038/s41586-021-03819-2.
920 27. Bieger, B., Essen, L.-O. & Oesterhelt, D. Crystal Structure of Halophilic Dodecin: A Novel,
921 Dodecameric Flavin Binding Protein from Halobacterium salinarum. *Structure* **11**, 375–
922 385 (2003).
923 28. Vallese, F. *et al.* Helicobacter pylori antigenic Lpp20 is a structural homologue of Tipα and
924 promotes epithelial-mesenchymal transition. *Biochimica et Biophysica Acta (BBA) -*
925 *General Subjects* **1861**, 3263–3271 (2017).
926 29. Zarzecka, U. *et al.* Functional analysis and cryo-electron microscopy of
927 Campylobacterjejuni serine protease HtrA. *Gut Microbes* **12**, 1–16 (2020).
928 30. Harris, B. Z. & Lim, W. A. Mechanism and role of PDZ domains in signaling complex
929 assembly. *J Cell Sci* **114**, 3219–3231 (2001).

930 31. Lee, H.-J. & Zheng, J. J. PDZ domains and their binding partners: structure, specificity,
931 and modification. *Cell Communication and Signaling* **8**, 8 (2010).
932 32. McDonald, J. B. *et al.* Characterisation of N-linked protein glycosylation in the bacterial
933 pathogen Campylobacter hepaticus. *Sci Rep* **13**, 227 (2023).
934 33. Blatch, G. L. & Lässle, M. The tetratricopeptide repeat: a structural motif mediating protein-
935 protein interactions. *BioEssays* **21**, 932–939 (1999).
936 34. D'Andrea, L. D. & Regan, L. TPR proteins: the versatile helix. *Trends in Biochemical*
937 *Sciences* **28**, 655–662 (2003).
938 35. Gao, B., Lara-Tejero, M., Lefebre, M., Goodman, A. L. & Galán, J. E. Novel Components
939 of the Flagellar System in Epsilonproteobacteria. *mBio* **5**, e01349-14 (2014).
940 36. Scott, N. E. *et al.* Simultaneous Glycan-Peptide Characterization Using Hydrophilic
941 Interaction Chromatography and Parallel Fragmentation by CID, Higher Energy Collisional
942 Dissociation, and Electron Transfer Dissociation MS Applied to the N-Linked
943 Glycoproteome of Campylobacter jejuni*. *Molecular & Cellular Proteomics* **10**, S1–S18
944 (2011).
945 37. Tachiyama, S. *et al.* The flagellar motor protein FliL forms a scaffold of circumferentially
946 positioned rings required for stator activation. *Proc Natl Acad Sci U S A* **119**, e2118401119
947 (2022).
948 38. Guo, S., Xu, H., Chang, Y., Motaleb, M. A. & Liu, J. FliL ring enhances the function of
949 periplasmic flagella. *Proceedings of the National Academy of Sciences* **119**, e2117245119
950 (2022).
951 39. Lynch, M. J. *et al.* Co-Folding of a FliF-FliG Split Domain Forms the Basis of the MS:C
952 Ring Interface within the Bacterial Flagellar Motor. *Structure* **25**, 317–328 (2017).
953 40. Lee, L. K., Ginsburg, M. A., Crovace, C., Donohoe, M. & Stock, D. Structure of the torque
954 ring of the flagellar motor and the molecular basis for rotational switching. *Nature* **466**,
955 996–1000 (2010).

956 41. Reid, S. W. *et al.* The maximum number of torque-generating units in the flagellar motor
957 of Escherichia coli is at least 11. *Proc. Natl. Acad. Sci. U.S.A.* **103**, 8066–8071 (2006).
958 42. Krachler, A. M., Sharma, A., Cauldwell, A., Papadakos, G. & Kleanthous, C. TolA
959 Modulates the Oligomeric Status of YbgF in the Bacterial Periplasm. *Journal of Molecular*
960 *Biology* **403**, 270–285 (2010).
961 43. Skórko-Glonek, J., Wawrzynów, A., Krzewski, K., Kurpierz, K. & Lipińiska, B. Site-directed
962 mutagenesis of the HtrA(DegP) serine protease, whose proteolytic activity is
963 indispensable for *Escherichia coli* survival at elevated temperatures. *Gene* **163**, 47–52
964 (1995).
965 44. Terashima, H. *et al.* Insight into the assembly mechanism in the supramolecular rings of
966 the sodium-driven Vibrio flagellar motor from the structure of FlgT. *PNAS* **110**, 6133–6138
967 (2013).
968 45. Engelhardt, H., Schuster, S. & Baeuerlein, E. An archimedian spiral: the basal disk of the
969 Wolinella flagellar motor. *Science (New York, N.Y.)* **262**, 1046–1048 (1993).
970 46. Nirody, J. A., Berry, R. M. & Oster, G. The Limiting Speed of the Bacterial Flagellar Motor.
971 *Biophysical Journal* **111**, 557–564 (2016).
972 47. Sato, K., Nakamura, S., Kudo, S. & Toyabe, S. Evaluation of the Duty Ratio of the Bacterial
973 Flagellar Motor by Dynamic Load Control. *Biophysical Journal* **116**, 1952–1959 (2019).
974 48. Sangermani, M., Hug, I., Sauter, N., Pfohl, T. & Jenal, U. Tad Pili Play a Dynamic Role in
975 Caulobacter crescentus Surface Colonization. *mBio* **10**, e01237-19 (2019).
976 49. Toro, E., Hong, S.-H., McAdams, H. H. & Shapiro, L. Caulobacter requires a dedicated
977 mechanism to initiate chromosome segregation. *Proc Natl Acad Sci U S A* **105**, 15435–
978 15440 (2008).
979 50. Senf, F., Tommassen, J. & Koster, M. Polar secretion of proteins via the Xcp type II
980 secretion system in Pseudomonas aeruginosa. *Microbiology (Reading)* **154**, 3025–3032
981 (2008).

982 51. Kozaeva, E., Nieto-Domínguez, M., Tang, K. K. Y. & Nikel, P. I. Leveraging engineered
983 Pseudomonas putida minicells for bioconversion of organic acids into short-chain methyl
984 ketones. 2024.01.06.574483 Preprint at https://doi.org/10.1101/2024.01.06.574483
985 (2024).
986 52. Müller, A. *et al.* Ultrastructure and complex polar architecture of the human pathogen
987 Campylobacter jejuni. *Microbiologyopen* **3**, 702–710 (2014).
988 53. Chen, S. *et al.* Structural diversity of bacterial flagellar motors. *EMBO J* **30**, 2972–2981
989 (2011).
990 54. Schuhmacher, J. S., Thormann, K. M. & Bange, G. How bacteria maintain location and
991 number of flagella? *FEMS Microbiology Reviews* **39**, 812–22 (2015).
992 55. Hendrixson, D. R., Akerley, B. J. & DiRita, V. J. Transposon mutagenesis of
993 Campylobacter jejuni identifies a bipartite energy taxis system required for motility.
994 *Molecular Microbiology* **40**, 214–224 (2001).
995 56. Cohen, E. J. *et al.* Campylobacter jejuni motility integrates specialized cell shape, flagellar
996 filament, and motor, to coordinate action of its opposed flagella. *PLOS Pathogens* **16**,
997 e1008620 (2020).
998 57. Van Vliet, A. H. M., Wood, A. C., Wooldridge, K., Ketley, J. M. & Henderson, J. 7.7 Genetic
999 Manipulation of Enteric Campylobacter Species. in *Methods in Microbiology* (eds.
1000 Williams, P., Ketley, J. & Salmond, G.) vol. 27 407–419 (Academic Press, 1998).
1001 58. Dugar, G. *et al.* The CsrA-FliW network controls polar localization of the dual-function
1002 flagellin mRNA in Campylobacter jejuni. *Nat Commun* **7**, 11667 (2016).
1003 59. Alzheimer, M. *et al.* A three-dimensional intestinal tissue model reveals factors and small
1004 regulatory RNAs important for colonization with Campylobacter jejuni. *PLOS Pathogens*
1005 **16**, e1008304 (2020).
1006 60. Dugar, G. *et al.* CRISPR RNA-Dependent Binding and Cleavage of Endogenous RNAs by
1007 the Campylobacter jejuni Cas9. *Molecular Cell* **69**, 893-905.e7 (2018).

1008 61. Corcoran, C. P. *et al.* Superfolder GFP reporters validate diverse new mRNA targets of
1009 the classic porin regulator, MicF RNA. *Molecular Microbiology* **84**, 428–445 (2012).
1010 62. Zheng, S. Q. *et al.* MotionCor2: anisotropic correction of beam-induced motion for
1011 improved cryo-electron microscopy. *Nat Methods* **14**, 331–332 (2017).
1012 63. Scheres, S. H. W. RELION: implementation of a Bayesian approach to cryo-EM structure
1013 determination. *J Struct Biol* **180**, 519–530 (2012).
1014 64. Zivanov, J. *et al.* New tools for automated high-resolution cryo-EM structure determination
1015 in RELION-3. *eLife* **7**, e42166 (2018).
1016 65. Rohou, A. & Grigorieff, N. CTFFIND4: Fast and accurate defocus estimation from electron
1017 micrographs. *J. Struct. Biol.* **192**, 216–221 (2015).
1018 66. Pettersen, E. F. *et al.* UCSF Chimera—A visualization system for exploratory research
1019 and analysis. *Journal of Computational Chemistry* **25**, 1605–1612 (2004).
1020 67. Goddard, T. D., Huang, C. C. & Ferrin, T. E. Visualizing density maps with UCSF Chimera.
1021 *J. Struct. Biol* **157**, 281–287 (2007).
1022 68. Pintilie, G. D., Zhang, J., Goddard, T. D., Chiu, W. & Gossard, D. C. Quantitative analysis
1023 of cryo-EM density map segmentation by watershed and scale-space filtering, and fitting
1024 of structures by alignment to regions. *J Struct Biol* **170**, 427–438 (2010).
1025 69. Ramlaul, K., Palmer, C. M. & Aylett, C. H. S. A Local Agreement Filtering Algorithm for
1026 Transmission EM Reconstructions. *Journal of Structural Biology* **205**, 30–40 (2019).
1027 70. Burnley, T., Palmer, C. M. & Winn, M. Recent developments in the CCP-EM software
1028 suite. *Acta Cryst D* **73**, 469–477 (2017).
1029 71. Kremer, J., Mastronarde, D. & McIntosh, J. Computer visualization of three-dimensional
1030 image data using IMOD. *Journal of structural biology* **116**, 71–76 (1996).
1031 72. Agulleiro, J.-I. & Fernandez, J.-J. Tomo3D 2.0 – Exploitation of Advanced Vector
1032 eXtensions (AVX) for 3D reconstruction. *Journal of Structural Biology* **189**, 147–152
1033 (2015).

1034 73. Castaño-Díez, D., Kudryashev, M., Arheit, M. & Stahlberg, H. Dynamo: a flexible, user-
1035 friendly development tool for subtomogram averaging of cryo-EM data in high-
1036 performance computing environments. *J. Struct. Biol.* **178**, 139–151 (2012).
1037 74. Nicastro, D. *et al.* The Molecular Architecture of Axonemes Revealed by Cryoelectron
1038 Tomography. *Science* **313**, 944–948 (2006).
1039 75. Mirdita, M. *et al.* ColabFold: making protein folding accessible to all. *Nat Methods* **19**, 679–
1040 682 (2022).
1041 76. Croll, T. I. ISOLDE: a physically realistic environment for model building into low-resolution
1042 electron-density maps. *Acta Cryst D* **74**, 519–530 (2018).
1043 77. Afonine, P. V. *et al.* New tools for the analysis and validation of cryo-EM maps and atomic
1044 models. *Acta Cryst D* **74**, 814–840 (2018).
1045 78. Gibson, D. G. *et al.* Enzymatic assembly of DNA molecules up to several hundred
1046 kilobases. *Nature Methods* **6**, 343–345 (2009).
1047 79. Froger, A. & Hall, J. E. Transformation of plasmid DNA into E. coli using the heat shock
1048 method. *J Vis Exp* 253 (2007) doi:10.3791/253.
1049 80. Boll, J. M. & Hendrixson, D. R. A Regulatory Checkpoint during Flagellar Biogenesis in
1050 Campylobacter jejuni Initiates Signal Transduction To Activate Transcription of Flagellar
1051 Genes. *mBio* **4**, e00432-13 (2013).
1052 81. Johnson, T. L., Scott, M. E. & Sandkvist, M. Mapping Critical Interactive Sites within the
1053 Periplasmic Domain of the Vibrio cholerae Type II Secretion Protein EpsM. *Journal of*
1054 *Bacteriology* **189**, 9082–9089 (2007).
1055
1056

1057 # Figures and legends

Figure 1

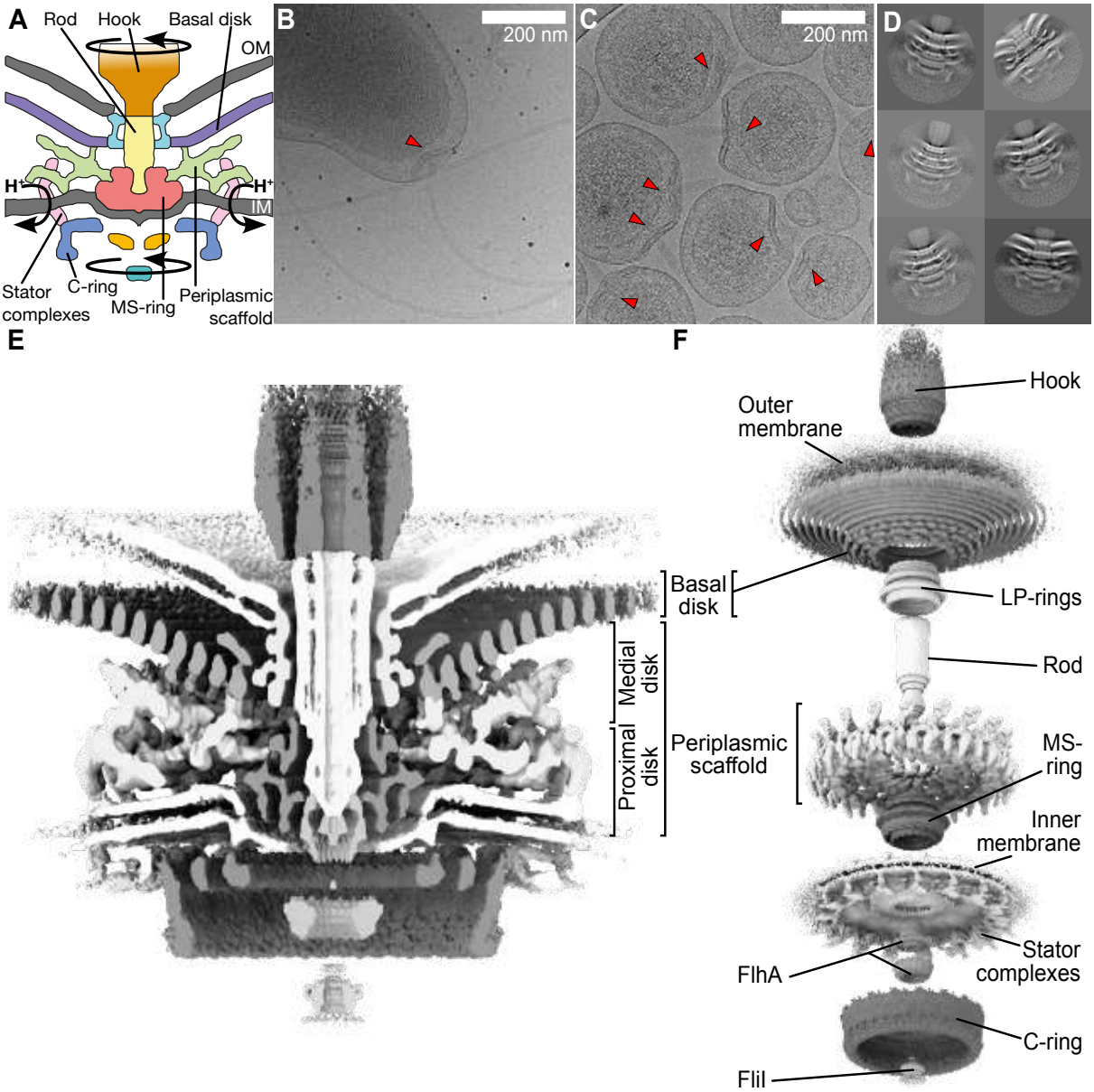

1058

1059 **Figure 1. Engineering of homogenous *Campylobacter jejuni* minicells enabled us to**
1060 **determine the *in situ* structure of a flagellar motor by single particle analysis electron**
1061 **cryo-microscopy (A) Schematic of the flagellar motor from *C. jejuni.* Proton flux through**
1062 **the stator complexes drives rotation of the C-ring, MS-ring, rod, and hook/filament. In**
1063 ***C. jejuni* and other Campylobacterota, a basal disk and periplasmic scaffold have**
1064 **evolved that scaffold a wider ring of additional stator complexes thought to be increase**
1065 **motor torque. IM/OM: inner/outer membrane (B) wildtype *C. jejuni* cells typically provide**
1066 **1 flagellar motor per field of view (arrowhead) as compared to (C) many motors per field**
1067 **of view in our minicell strain (arrowheads), greatly increasing throughput and reducing**
1068 **sample thickness for higher quality electron micrograph acquisition. Note that**
1069 **curvature of minicells is comparable to wildtype cells (D) Periplasmic and cytoplasmic**
1070 **features are evident in single particle analysis 2-D classes of manually picked motors.**
1071 **(E) Cross-section through an isosurface rendering of a C17 whole-motor 3-D**
1072 **reconstruction. (F) Map from (E), segmented and exploded along the z-axis to highlight**
1073 **component structures.**

Figure 2

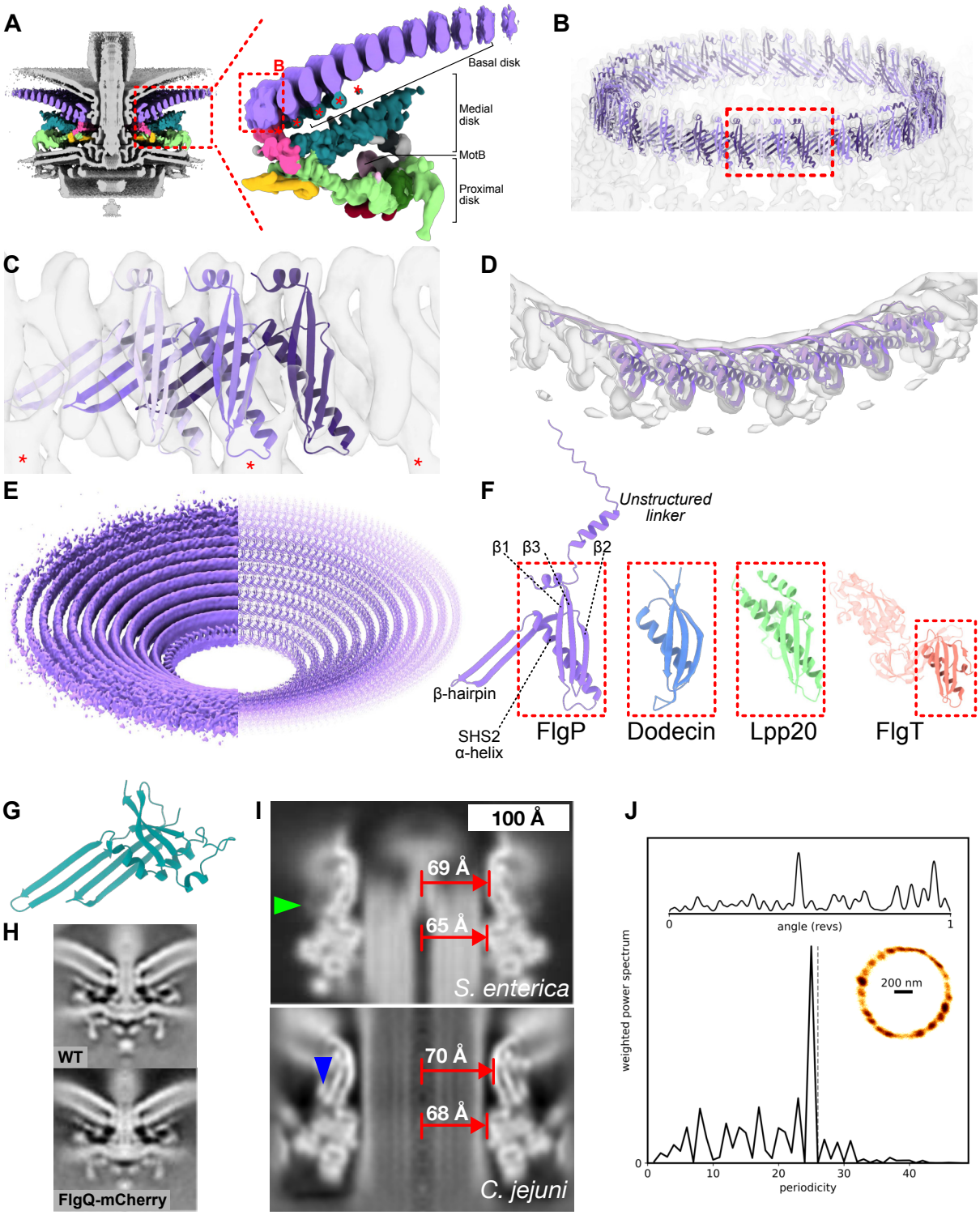

1074

1075 **Figure 2. The basal disk is comprised of many concentric rings of FlgP that encircle the**
1076 **LP-rings. (A) Focused C17 refinement of the periplasmic scaffold and inner ring of the**
1077 **basal disk shows that the scaffold attaches to the innermost ring of the basal disk,**
1078 **which itself is a series of concentric rings. Different sections of the periplasmic scaffold**
1079 **and basal disk in colour. (Right) One asymmetric unit of the periplasmic scaffold**
1080 **structure in side view highlighting components. Asterisks denote additional densities**
1081 **attached beneath the first five rings of the basal disk. Note that second and subsequent**
1082 **rings of the basal disk were not part of the focused refinement. (B) The innermost basal**
1083 **disk ring fits 51 FlgP monomers as 17 trimeric protomers (C) Fit of a FlgP trimer into**
1084 **density. Each protomer interacts with the 17-fold symmetric density of the medial disk**
1085 **(asterisks). (D) Top view of a fit of seven FlgP monomers into density map. (E) Density**
1086 **of 10 concentric rings (left) and fitted models (right). (F) FlgP has an unstructured N-**
1087 **terminal linker followed by an SHS2-like fold exemplified by dodecin (PDBID: 1MOG),**
1088 **and shared with Lpp20 of *Helicobacter pylori* (PDBID: 5OK8) and FlgT of *Vibrio***
1089 ***alginolyticus* (PDBID: 3W1E). All are OM-associated and FlgT is a flagellar component,**
1090 **indicating shared evolutionary origin. (G) AlphaFold model of FlgQ with signal**
1091 **sequence removed has a double β-hairpin that resembles a two-protomer repeat of**
1092 **FlgP. (H) Tagging FlgQ with mCherry, the resulting motor is indistinguishable from WT.**
1093 **(I) The *Campylobacter jejuni* LP-rings have comparable diameters to the 26-fold**
1094 **symmetric *Salmonella enterica* serovar Typhimurium LP-rings. The density map of the**
1095 ***Salmonella* LP-rings (EMD-12183) was low-pass filtered to 15 Å-resolution and lathed**
1096 **to enable like-for-like comparison with the *C. jejuni* LP-rings. The *Salmonella* L- and P-**
1097 **rings are 69 Å and 65 Å diameter, compared to 70 Å and 68 Å in *C. jejuni* Green**
1098 **arrowhead indicates the location of *Salmonella* YecR; blue arrowhead indicates the**
1099 **location of unidentified *C. jejuni* density. (J) Support for the *C. jejuni* LP-rings having**
1100 **comparable stoichiometry to *E. coli* and *Salmonella* from detection of close to 26 steps**
1101 **in flagellar rotation. Top: kernel density estimation of bead position as a function of**
1102 **rotational angle. Bottom: weighted power spectrum of angular position; grey dashed**
1103 **line marks 26 to guide the eye; this example is most consistent with 25 steps. Inset: x,y-**
1104 **position histogram with density represented by darkness of coloration. See Extended**
1105 **Data Fig. 4 for ten other traces.**

Figure 3

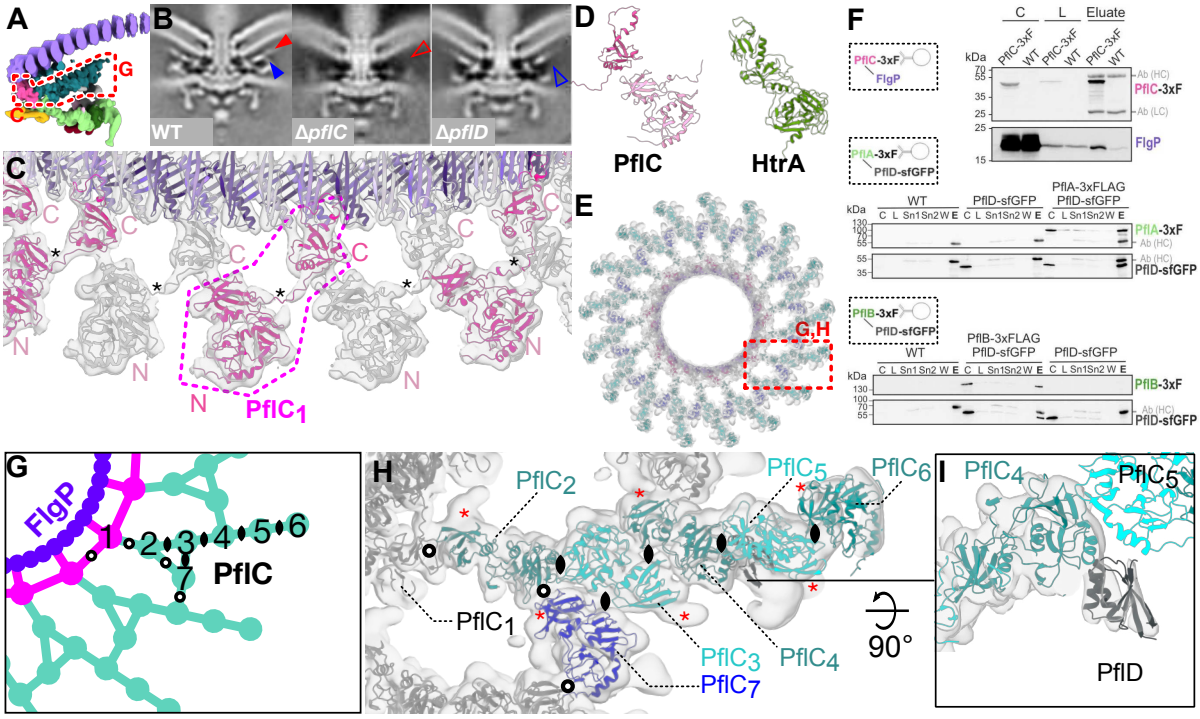

Figure 3. The medial disk is composed of a lattice of previously-unidentified PflC, decorated with PflD and interacts with the basal and proximal disks. (A) The medial disk is situated between the basal disk and proximal disk. (B) Comparing the WT motor structure (from EMD-3150) to a *pflC* deletion reveals abolished assembly of the medial disk (empty red arrowhead; filled red arrowhead on WT structure), while *pflD* deletion abolishes assembly of a post-like density between the medial and proximal disks (empty blue arrowhead; filled blue arrowhead on WT structure). (C) An inner ring of 17 domain-swapped PflC protomers (alternating grey/pink) attach to every third FlgP in the 51-protomer inner ring of the basal disk (purple). A single PflC protomer (magenta outline) features domains from two proteins. Black asterisks denote location of the linker helix between two domains of one protein (D) Predicted structure of PflC highlights common folds and domain architecture with HtrA, a periplasmic protease. (E) Top view of the medial disk viewed from outside the cell. Every asymmetric unit (dashed red box) features seven PflC proteins and one PflD protein as further investigated in panels G and H. $PflC_1$ represented in pink as per panel C; $PflC_{2,4,6}$ in teal; $PflC_{3,5}$ in cyan; $PflC_7$ in blue. (F) PflC and PflD interact with known flagellar disk structure components: (top) Western blot analysis of coIP experiment of PflC-3xFLAG. As control, untagged wild-type cells (WT) were used. Detected heavy (HC) and light (LC) antibody chains are indicated. C: culture; L: lysate. (middle) Western blot analysis of coIP experiment of PflA-3xFLAG, PflD-sfGFP double tagged strain. As controls, PflD-sfGFP and untagged wild-type (WT) cells were used. Detected heavy (HC) antibody

1128 **chains are indicated. C: culture; L: lysate; Sn1/2: supernatant 1/2; W: wash; E: eluate.**
1129 **(bottom) Western analysis of coIP experiment of PflB-3xFLAG, PflD-sfGFP double**
1130 **tagged strain. As controls, PflD-sfGFP and untagged wild-type cells were used.**
1131 **Detected heavy (HC) antibody chains are indicated. C: culture; L: lysate; Sn1/2:**
1132 **supernatant 1/2;W: wash; E: eluate. (G) Schematic illustrating the differential**
1133 **oligomerisation of PflC protomers within the medial disk's lattice. Twofold symmetry**
1134 **axis symbols highlight symmetric dimerization interfaces with axes approximately**
1135 **perpendicular to the plane of the lattice; empty circles represent asymmetric interfaces.**
1136 **Three equivalent twofolds exist: 2:3 and 4:5; 3:4 and 5:6; and 3:7, although the 3:7**
1137 **interface is substantially warped (H) Molecular model of the PflC lattice fitted in our**
1138 **density map denoting symmetry elements relating monomers enlarged from red box in**
1139 **panel E. Densities adjacent to every Asn239 denoted by red asterisks correspond to an**
1140 **established glycosylation site of a PflC from a closely-related species. Symmetry**
1141 **elements as per panel F. (I) side view depicting PflD sitting beneath $PflC_{4,5}$.**

1142

Figure 4

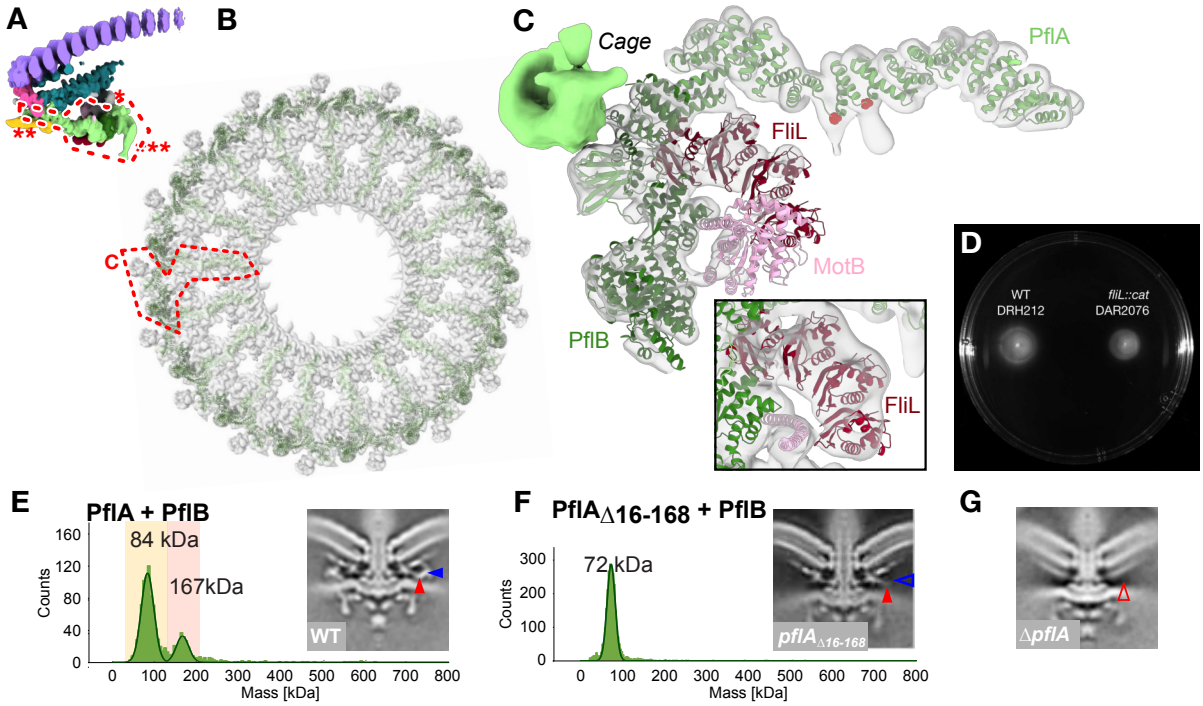

Figure 4. PflA and PflB form a spoke-and-rim structure that scaffolds 17 stator complexes. (A) Location of the proximal disk in the periplasmic scaffold denoted by dashed red line. Asterisks denote unassigned densities: the PflD-adjacent density (*), E-ring (**), and peripheral cage (***) (B) Top view of the 17-fold symmetric proximal disk. Dashed red box denotes the asymmetric unit illustrated in panel C. (C) Every asymmetric unit features one PflA, one PflB, an arc of four FliL, and one stator complex (itself composed of five copies of transmembraneous MotA and two copies of periplasmic MotB). PflA (light green) is positioned radially like spokes, interacting at its N-terminal end with a rim of PflB (dark green) at the outer edge of the scaffold. An arc of FliL (red) and periplasmic domain of MotB (pink, residues 68-247) are also evident at lower confidence. Inset: focus on FliL at lower threshold to demonstrate match of four FliL models into four periodic densities. (D) Deletion of fliL has only a minor effect on motility. A representative motility agar plate stabbed with WT and *fliL::cat* demonstrates that fliL knockout has only a minor effect on motility. (E) Mass photometry measurements confirm the PflAB dimer (red background) forms *in vitro*. Inset: 100 nm x 100 nm cross-section through the subtomogram average density map of the WT motor exhibits $PflA_C$ (filled red arrowhead) and PflB densities (filled blue arrowhead). Structure from EMD-3150. (F) Mass photometry shows that deleting the PflA β-sandwich and linker abolishes dimerization with PflB. Inset: 100 nm x 100 nm cross-section through a density map of the subtomogram average of this mutant reveals a vestigial $PflA_C$ density (filled red arrowhead) and loss of PflB (empty blue arrowhead),

1165 **whereas (G) a 100 nm x 100 nm cross-section through a density map of the**
1166 **subtomogram average of a PflA deletion further lacks the vestigial $PflA_C$ density (empty**
1167 **red arrowhead) (structure from EMD-3160).**

1168

Figure 5

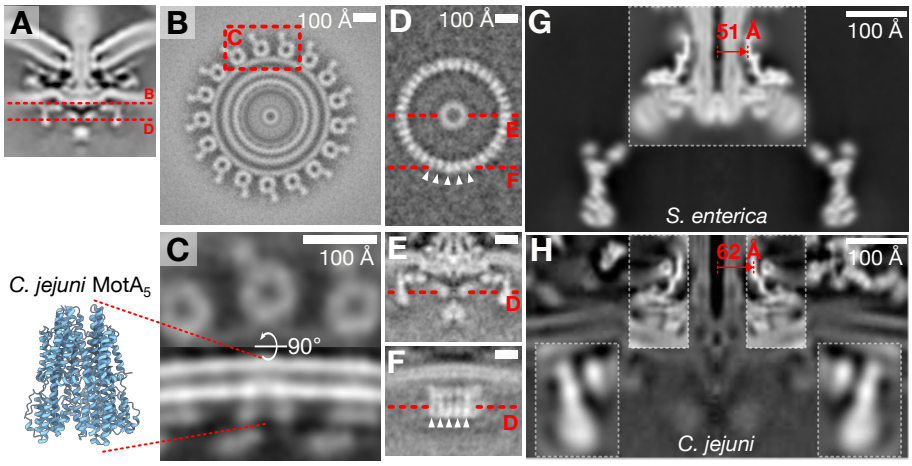

Figure 5. Wider rings of additional stator complexes are incorporated in the *Campylobacter jejuni* periplasmic scaffold while the rotor components are correspondingly wider. (A) Cross-section the wildtype *C. jejuni* motor depicting locations of stator and rotor cross-sections illustrated in panels B and D. (B) Cross-section through the whole-motor map just beneath the outer membrane shows 17 circular densities at the expected location of MotA. (C) A focused refinement of the stator complexes reveals pentameric densities, that (C) In cross-section have the distinctive thimble-like shape of a MotA pentamer, from PDB 6ykm. (D) Cross-section through the *C. jejuni* C-ring showing 38-fold periodic structure. Arrowheads highlight 5 of the 38 puncta. Labels (E) and (F) denote cross-sections depicted in respective panels. (E) Cross-section through the centre of the *C. jejuni* C-ring; (F) cross-section through the edge of the C-ring showing post-like densities corresponding to the periodicity shown in panel (D) (arrowheads) as have been reported in the *Salmonella* C-ring. (G) Cross-section through a composite map of the *Salmonella enterica* serovar Typhimurium MS-ring (from EMD-12195) and C-ring (from EMD-42439) rotor components depicting the 51 Å-radius MS-ring β-collar. Both maps were low-pass filtered to 15 Å-resolution and lathed around their rotational axis to allow like-for-like comparison with (H) cross-section through a composite map of the whole-motor *C. jejuni* map, with superimposed cross-sections through focused, lathed *C. jejuni* MS-ring and C-ring maps, highlighting the wider 62 Å-radius β-collar.

Figure 6

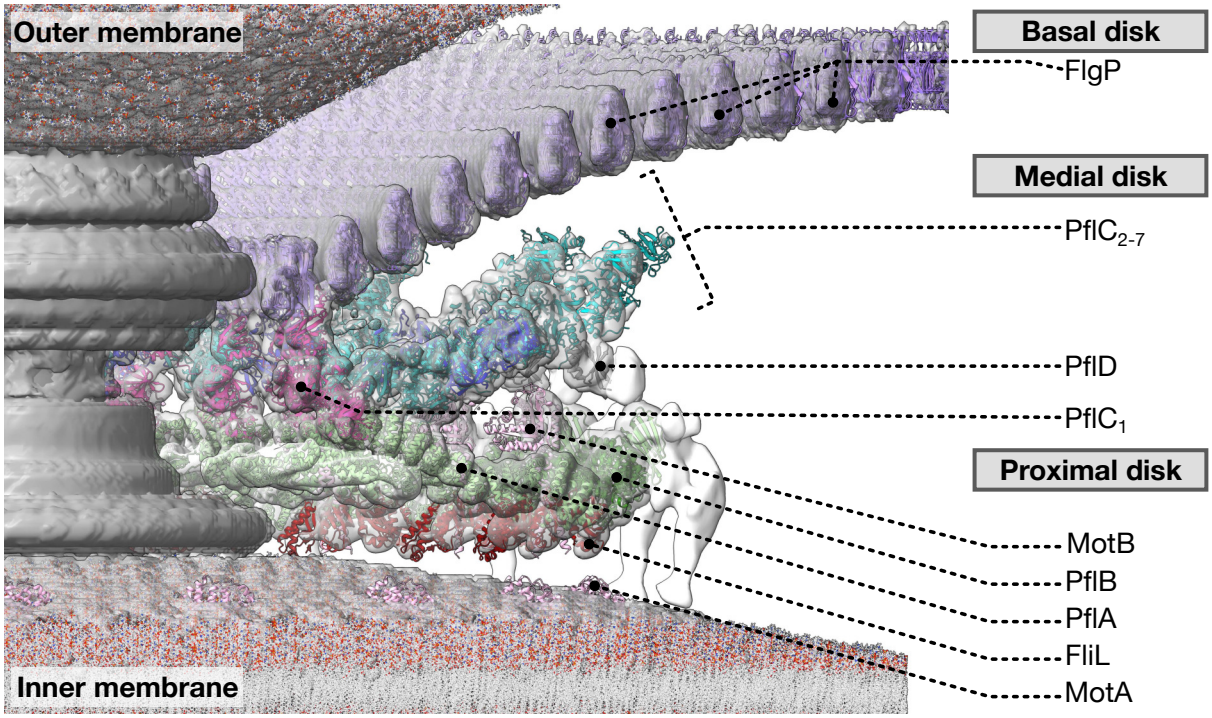

Figure 6. A "parts-list" of protein adaptations to increase torque by scaffolding a wider ring of additional stator complexes, thus exerting greater leverage on the axial flagellum. A partial-cutaway schematic of the structure of the *Campylobacter jejuni* flagellar motor contextualising protein components modelled in this study. The basal disk is formed of FlgP; the medial disk of PflC and PflD; the proximal disk of PflA, PflB, and FliL together with stator complex components MotA and MotB. Asterisks on transparent density denote unassigned densities: a PflD-adjacent density (*), E-ring (**), and peripheral cage (***).

Extended data figure legends

Extended Data Figure 1

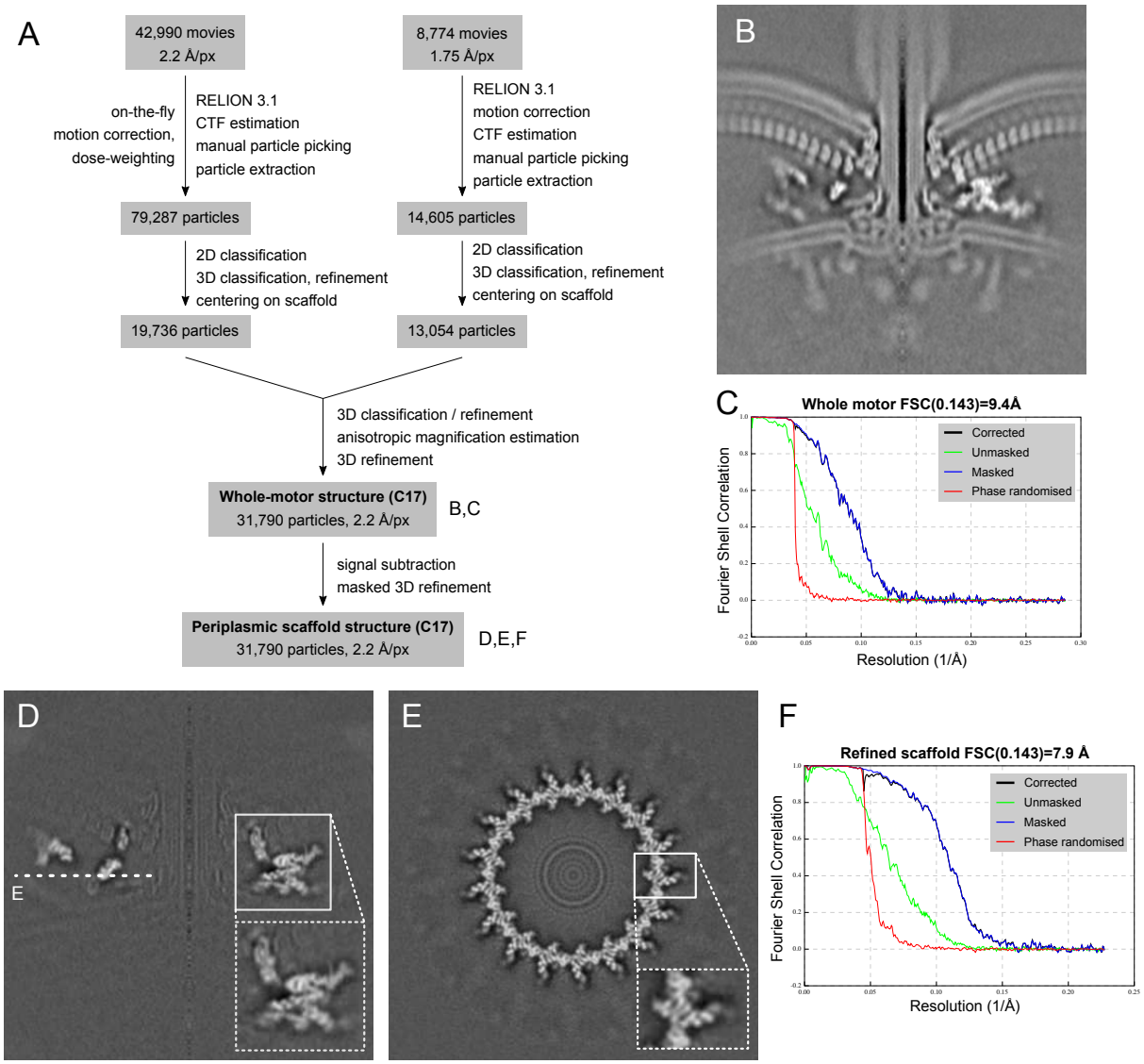

Extended Data Figure 1. Flowchart and resolution estimates of structure determination of the *Campylobacter jejuni* bacterial flagellar motor using in situ single particle analysis. (A) Simplified flowchart showing the generation of cryoEM volumes. (B) Central slice through the refined whole-motor structure. (C) FSC curve for B. (D) and (E) show slices through the volume of the refined, signal-subtracted periplasmic scaffold. (F) FSC curve for D, E.

Extended Data Figure 2

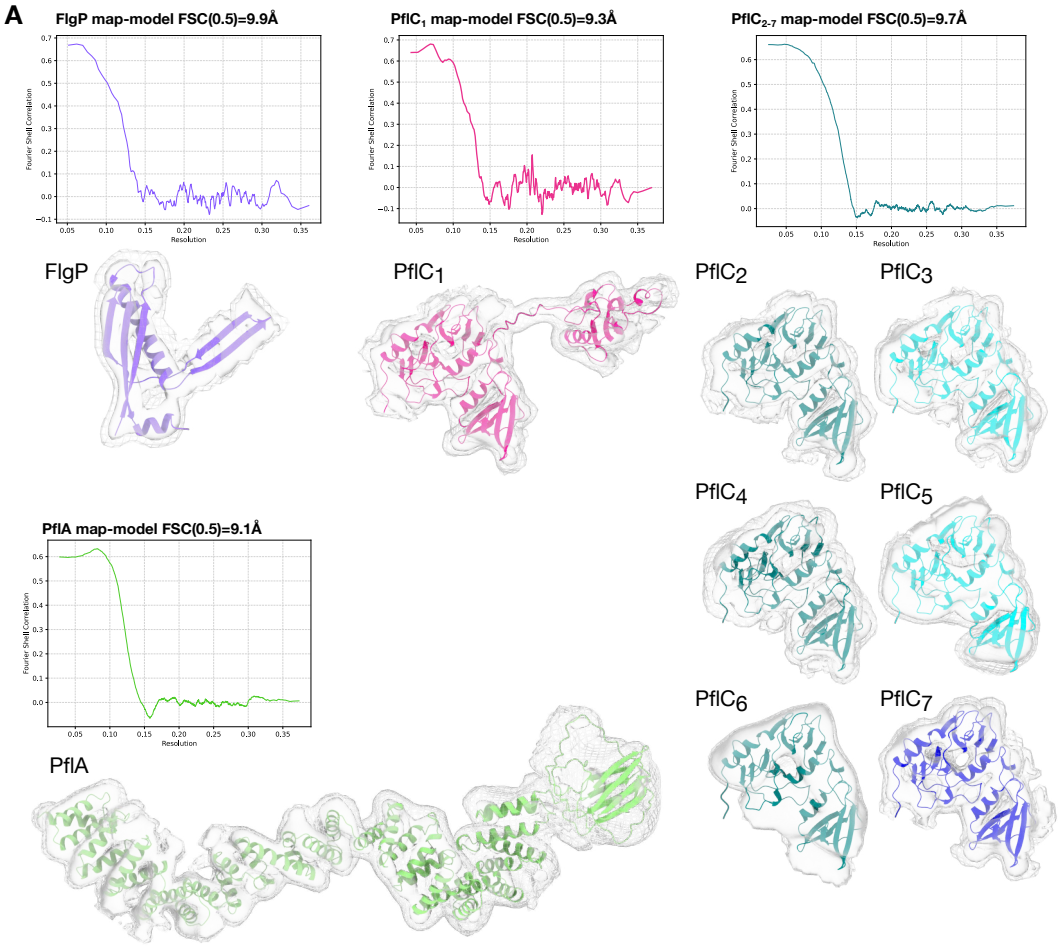

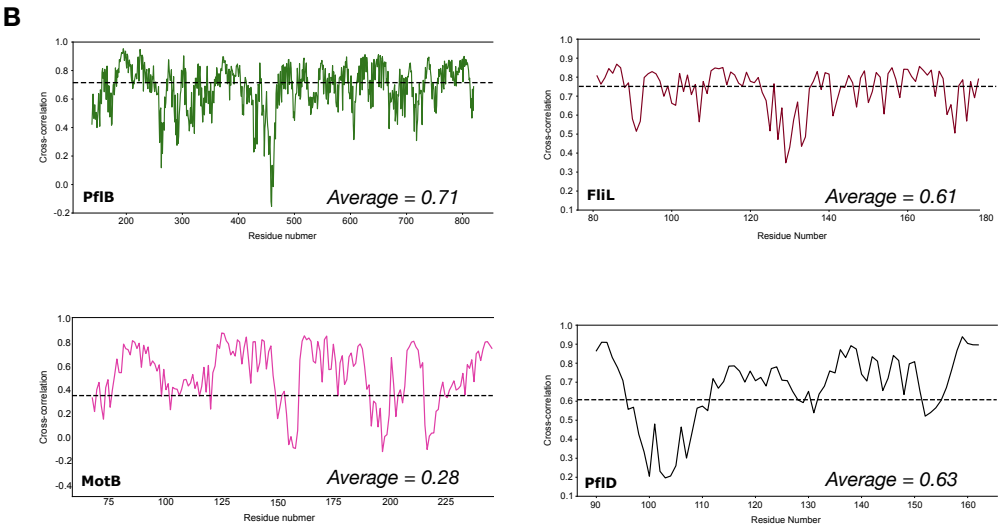

1210

1211 **Extended Data Figure 2. Validation of those protein chains modelled in the scaffold map**
1212 **to subnanometre resolution. (A) Map-model FSC curves for protein models refined into**
1213 **the scaffold map: FlgP, PflA, PflC$_1$, and PflC$_{2-7}$ calculated in Phenix, alongside images**
1214 **of excised pieces of the density map corresponding to individual proteins. High and**
1215 **low isosurface thresholds are denoted by solid and mesh surfaces, respectively, to**
1216 **illustrate fit of models into secondary structure densities. (B) Cross-correlation per**
1217 **residue plots of proteins docked into the map: PflB, FliL, MotB, PflD, calculated using**
1218 **Phenix. Mean CC values are shown with dashed line and in text inset.**

1219

Extended Data Figure 3

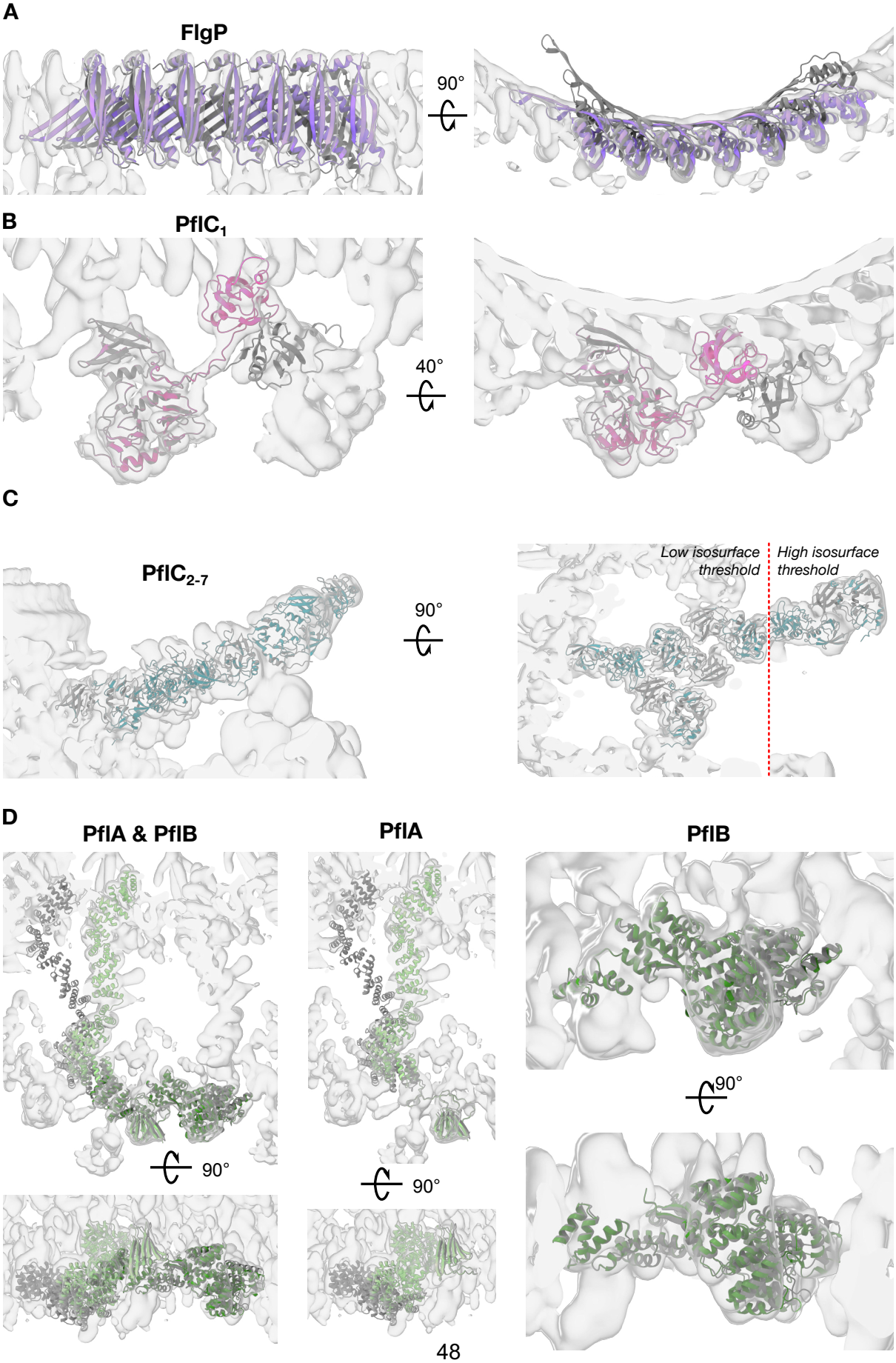

1221 **Extended Data Figure 3. Comparison of AlphaFold2 starting models with final**
1222 **structures after flexible fitting. (A) AlphaFold2 prediction of FlgP (dark grey) required**
1223 **bending of the oligomer to fit the curvature of the first ring of the basal disk (purple).**
1224 **(B) AlphaFold2 prediction of $PflC_1$ required independent rigid-body docking of the N-**
1225 **and C-terminal domains (magenta). (C) The resulting N-terminal domain of PflC was**
1226 **rigid-body docked into density multiple times for $PflC_{2-7}$. C-terminal domains were not**
1227 **modelled. Higher thresholds required for more peripheral, and presumably more**
1228 **flexible, components. (D) PflA and PflB AlphaFold2 models (dark grey) required**
1229 **bending to fit into density maps (pale and dark green for PflA and PflB, respectively).**

1230

Extended Data Figure 4

A

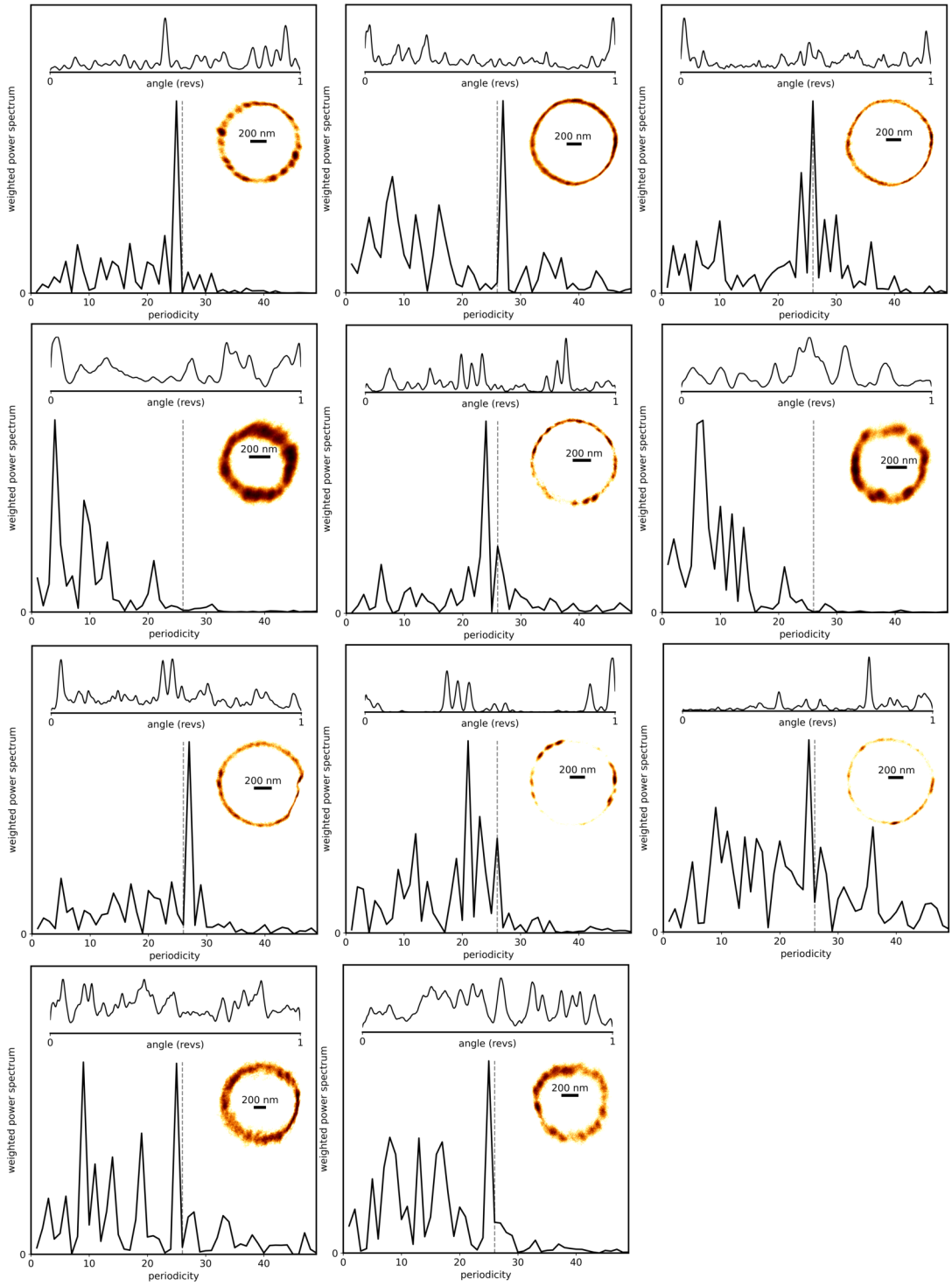

B

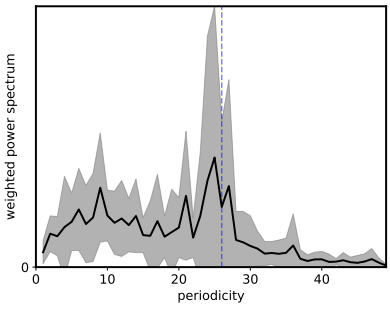

1232 **Extended Data Figure 4. Discrete steps in flagellar rotation are similar to those in *E.***
1233 ***coli.* (A) Kernel density estimation bead position plots over many rotations for 11 cells.**
1234 **Measurements were of duration 20 to 240 seconds, substantially de-energized by CCCP**
1235 **to slow rotation. Their (x,y) histograms, a kernel density of the angular position, and**
1236 **the weighted power spectrum are depicted. The top left is the trace shown in Fig. 2. (B)**
1237 **Weighted power spectrum of all 11 traces.**

1238

Extended Data Figure 5

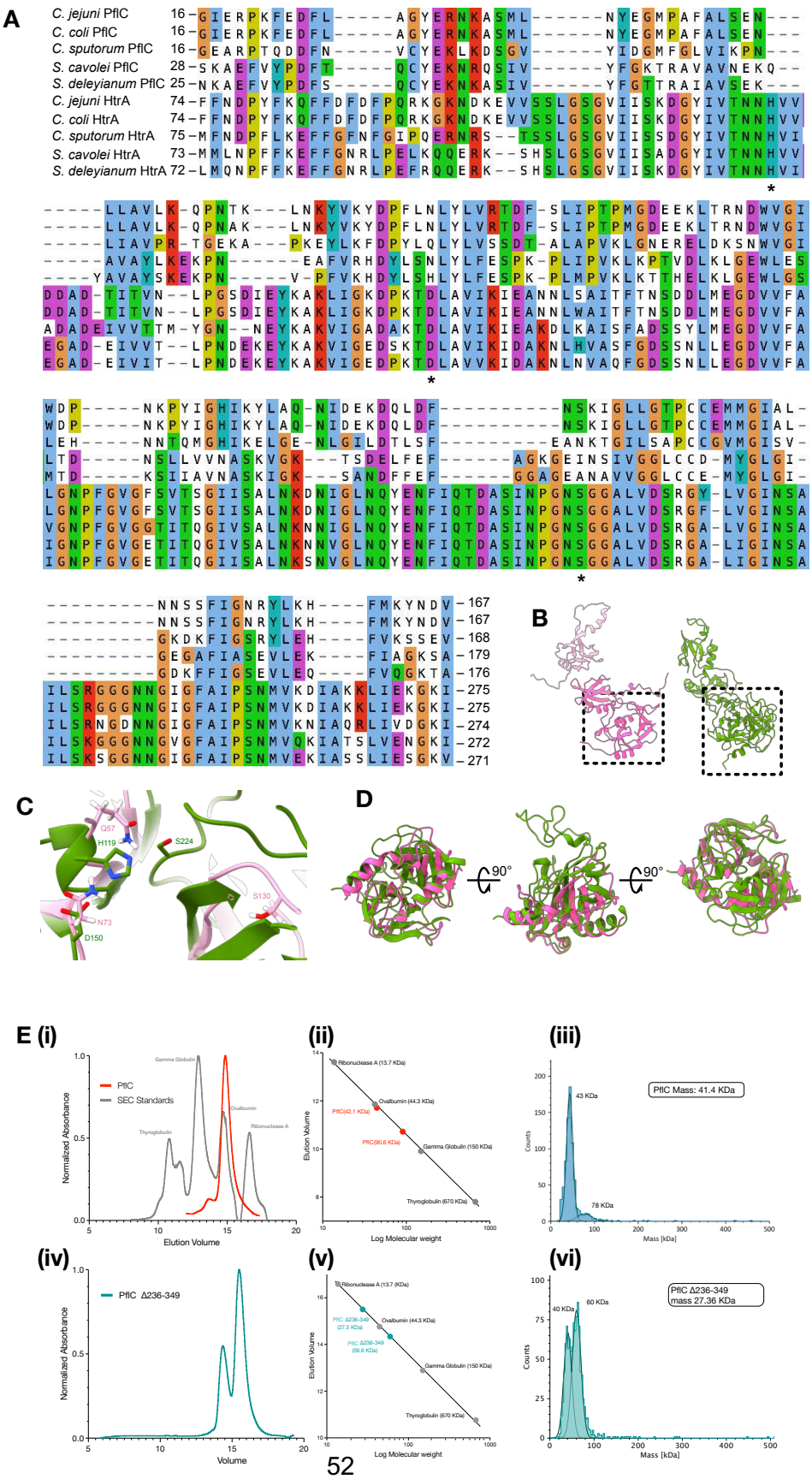

1239

1240 **Extended Data Figure 5. PflC (a previously unknown glycoprotein) resembles an**
1241 **inactivated HtrA that forms oligomerises *in vitro,* regulated by its C-terminal PDZ**
1242 **domain. (A) Multiple sequence alignment of PflC and HtrA protease domains from**
1243 **species in the sister clades *Campylobacter* and *Sulfurospirillum*. Alignment is based**
1244 **on structural alignments of PflC and HtrA models, with local sequence re-alignments.**
1245 **Asterisks highlight catalytic triad residue locations that are conserved as His-Asp-Ser**
1246 **in HtrA but not PflC. (B) Structurally aligned PflC (left) and HtrA (right), highlighting**
1247 **location of the protease domain. (C) The His-Asp-Ser catalytic triad in the protease**
1248 **domain of HtrA (green) is not conserved in PflC (pink). (HtrA PDBID: 6Z05). (D)**
1249 **Structural alignment of the HtrA domains of HtrA and PflC in ChimeraX Matchmaker.**
1250 **RMSD between pruned atom pairs 1.3 Å, across all atoms 10.4 Å. (E) Oligomerisation**
1251 **of PflC is regulated by its C-terminal domain: (i) Size Exclusion Chromatography of PflC**
1252 **(red) along with protein standards (grey) showing elution volume. (ii) Calibration graph**
1253 **showing a dimer of PflC (red) corresponding to retention times during elution. (iii) Mass**
1254 **photometry measurements of purified PflC (replicates). (iv) Size Exclusion**
1255 **Chromatography of PflCN (Δ236-349, green) along with protein standards (grey)**
1256 **showing elution volume. (v) Calibration graph of PflCN (green) corresponding to**
1257 **retention times during elution. (vi) Mass photometry measurements of purified PflCN.**
1258 **Theoretical masses are shown in the inserts. The instrument's limit of detection is 35**
1259 **kDA, meaning the monomer mass is larger than otherwise expected.**

1260

Extended Data Figure 6

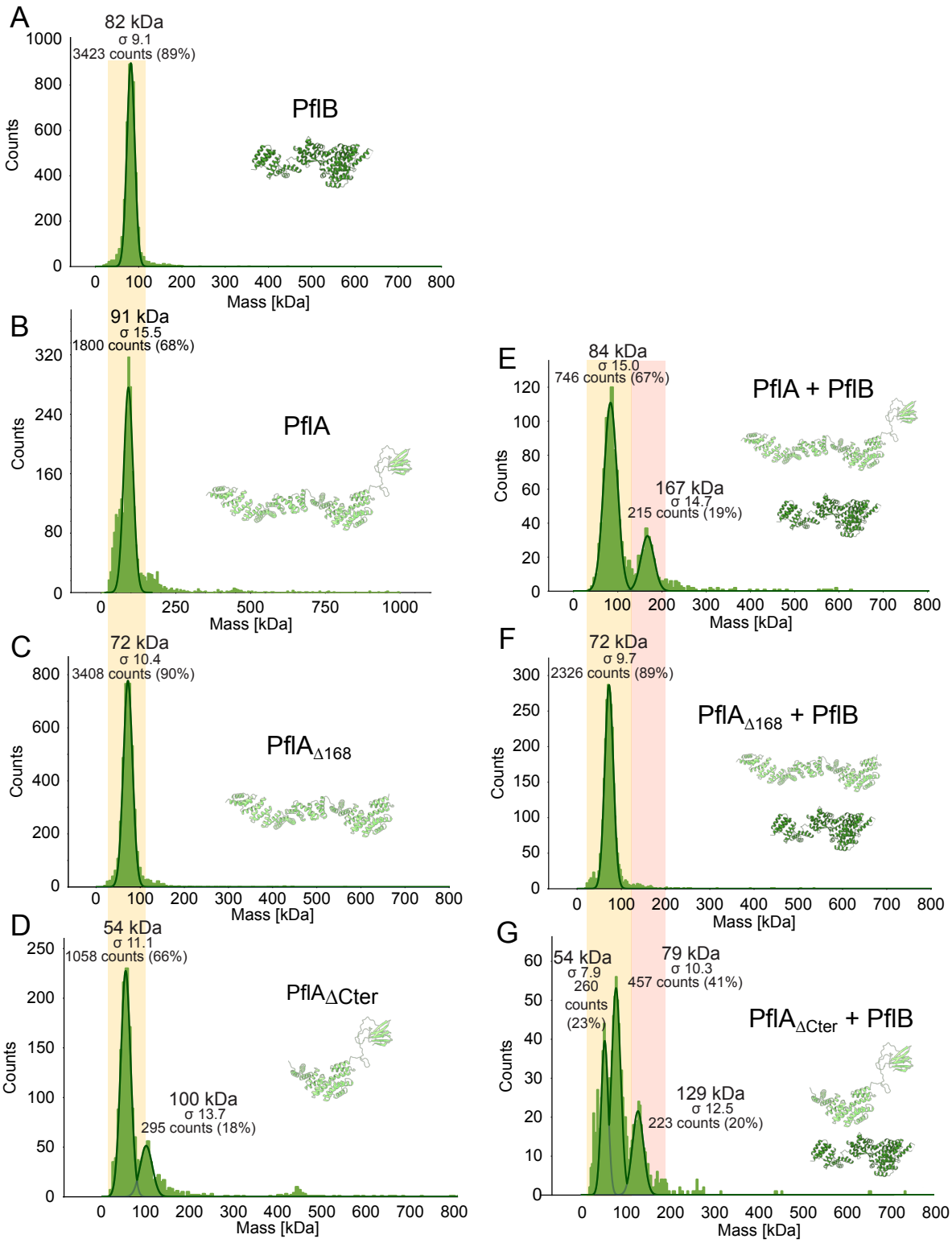

1261

1262 **Extended Data Figure 6. Mass photometry shows that PflA dimerises with PflB via its**
1263 **N-terminal β-sandwich domain. (A-D) Mass photometry measurements of purified PflA**
1264 **and PflB constructs show the proteins are mainly monodisperse. There is a dimer peak**
1265 **present for the $PflA_{\Delta Cter}$ construct, likely due to a reduction in stability and solubility.**
1266 **(E-G) Mass photometry measurements of mixtures of PflB and PflA variants. Dimer**
1267 **peaks appear only when β-sandwich and linker domain of PflA is present. In panels E**
1268 **and G, monomer peaks of PflA and PflB are not resolved due to their similar molecular**
1269 **weights. In the bottom panel, the 54 kDa peak corresponds to $PflA_{\Delta Cter}$, and the 79 kDa**
1270 **peak to PflB. Broadly, monomer peaks have a yellow background, dimer peaks red.**

1271

1272 # Tables with titles and legends

1273 **Table 1: Data collection statistics of two cryoEM data collection sessions.**

Parameter	Dataset 1 (“F3”)	Dataset 2 (“K2”)
Voltage (kV)	300	300
Detector	Falcon III	K2
Pixel size (Å/px)	1.75	2.2
Exposure dose per frame (e^-/Å/frame)	5	1.53
Total exposure dose (e^-/Å)	50	50
Defocus range (μm)	-1.5 to -3.0	-1.5 to -3.0
Total micrographs	8,774	42,988

1274 # Supplemental table titles

1275 **Table S1: PflA and PflB pulldowns and mass spectrometry**

1276 **Table S2: Structural components of the *Campylobacter jejuni* flagellar motor**

1277 **Table S3: Antisera, strains, and recombinant DNA used in this study**

1278 (*Files provided separately in XLSX format*)

TABLE S1

PflA co-immunoprecipitation results

Accession	Protein	% Coverage	# PSMs	Ratio Abundance (D*pflA*/*pflA-FLAG*/D*pflA*/vector)
A0A0H3PAU5	PflA	95	979	2.87E+03
A0A0H3PI11	Cjj81176_1608,	60	13	6.72E+02
A0A0H3P9Z2	Cjj81176_0859,	22	17	2.39E+02
A0A0H3PBX6	MotB	39	11	1.58E+02
A0A0H3PIR6	Cjj81176_0166 I	56	32	1.37E+02
Q29W27	KpsD, capsular p	27	29	9.38E+01
A0A0H3PAU1	PflD	33	4	7.26E+01
A0A0H3PBN5	Cjj81176_0293,	39	8	6.85E+01
A0A0H3PGP7	FlgE, flagellar ho	58	47	6.70E+01
A0A0H3PCN0	Cjj81176_0127,	58	36	5.97E+01
A0A0H3PJ87	PflB	91	581	5.76E+01
A0A0H3PJ16	ModA, molybde	27	6	4.76E+01
A0A0H3PCR9	Cjj81176_1227,	29	8	4.49E+01
A0A0H3PIF6	FliL	35	6	4.45E+01
A1VYV6	Cbf2, putative p	60	63	4.04E+01
A0A0H3P9I9	YchF, ribosome-	19	8	3.86E+01
A0A0H3PHE2	Cjj81176_0792,	17	9	3.50E+01
A0A0H3PC06	Cjj81176_0400,	11	2	3.17E+01
A0A0H3PEG3	FliO	44	18	2.96E+01
A0A0H3PDV4	Cjj81176_1419,	44	17	2.96E+01

Accession	Protein	% Coverage	# PSMs	Abundance in D*pflA*/*pflA-FLAG* *
A0A0H3P9L7	Cjj81176_0128,	26	16	5.10E+06
A0A0H3PEV8	PbpA, penicillin-	20	14	4.15E+06
A0A0H3PE83	PflC	37	13	9.45E+06
A0A0H3P9U7	JlpA, surface-exp	26	10	3.12E+05
A0A0H3PIX5	Cjj81176_0480,	27	7	2.29E+06

A0A0H3PHT3	Cjj81176_1375,	27	6	1.20E+06
A0A0H3PHU2	Cjj81176_1517,	11	5	4.58E+05
A0A0H3P9C0	Cjj81176_1195,	19	4	4.32E+05
A0A0H3PDG0	Cjj81176_0851,	9	3	6.13E+05
A0A0H3PBC1	Cjj81176_0178,	5	3	5.43E+05
A0A0H3PD23	Cjj81176_1105.	15	3	1.30E+05
A0A0H3PAF3	Cjj81176_0231 ,	25	3	1.14E+06
A0A0H3PEX7	Cjj81176_0438,	15	3	2.44E+05
A0A0H3PAT4	Cjj81176_1652,	3	2	6.99E+05
Q0Q7H1	AtpE, ATP synth	31	2	3.65E+05
A0A0H3P986	Cjj81176_0968,	8	2	5.18E+05
A1W170	FlgI	9	2	3.68E+05
A0A0H3PD29	CobB, NAD-depe	3	2	8.70E+04
A0A0H3PBM4	Cjj81176_0677,	21	2	3.98E+05
A0A0H3PAG3	SdhC, succinate	6	2	5.73E+05
A0A0H3PBJ5	DsbD, thiol:disul	5	2	5.00E+04
A0A0H3PIZ5	Cjj81176_0157,	4	2	1.88E+05
A0A0H3P9K1	Cjj81176_0815,	4	2	1.88E+05
A0A0H3PA19	Cjj81176_0835,	4	2	1.88E+05

* These proteins were not detected by mass spectrometry in D*pflA* /vector. Thus, no abundance ratios can be calcualted.

PflB co-immunoprecipitation results

Accession	Protein	% Coverage	# PSMs	Ratio Abundance (D*pflB*/*pflABFLAG*/D*pflB*/vector)
A0A0H3PJ87	PflB	91	581	2.39E+03
A0A0H3PIR6	Cjj81176_0166,	56	32	4.38E+02
A0A0H3PEG3	FliO	44	18	1.02E+02
A0A0H3P9H3	DsbA, thiol:disul	38	12	3.92E+01
Q29W27	KpsD, capsular p	27	29	3.83E+01
A0A0H3P9J8	CjaC protein	18	6	3.11E+01
A0A0H3PDV4	Cjj81176_1419,	44	17	2.81E+01
A0A0H3PAU5	PflA	95	979	2.59E+01

A0A0H3PCT8	Cjj81176_1302,	17	21	2.42E+01
A0A0H3PIF6	FliL	35	6	2.28E+01
A0A0H3PAR8	MltG, endolytic	18	8	1.61E+01
A1VYV6	Cbf2, putative p	60	63	1.49E+01
A0A0H3P9T5	Cjj81176_1649,	13	11	1.31E+01
A0A0H3PCN0	Cjj81176_0127,	58	36	1.14E+01
A0A0H3PG98	CJJ81176_pVir0	40	23	1.11E+01
A0A0H3PI11	Cjj81176_1608,	60	13	1.08E+01
A0A0H3PHN8	Cjj81176_0836,	50	16	1.07E+01
A0A0H3PJ16	ModA, molybde	27	6	1.03E+01
A0A0H3P9F0	PglF, general gly	11	7	8.41E+00
A0A0H3PA52	HtrA, periplasmi	40	22	8.24E+00

Accession	Protein	% Coverage	# PSMs	Abundance in D*pflA*/*pflA-FLAG* *
A0A0H3P9U7	JlpA, surface-exp	26	10	3.15E+06
A0A0H3P9L7	Cjj81176_0128,	26	16	2.62E+06
A0A0H3PEV8	PbpA, penicillin-	20	14	2.06E+06
A0A0H3PA77	Cjj81176_0918,	24	3	5.03E+05
A0A0H3PIX5	Cjj81176_0480,	27	7	3.95E+05
A0A0H3PHU2	Cjj81176_1517,	11	5	3.72E+05
A0A0H3PAZ8	Cjj81176_0160,	6	1	3.50E+05
A0A0H3PAJ6	Cjj81176_0479,	10	5	2.88E+05
A0A0H3PAH4	Cjj81176_0565,	22	4	2.53E+05
A0A0H3PJB7	SdhB, succinate	5	5	2.39E+05
A0A0H3PHT3	Cjj81176_1375,	27	6	2.04E+05
A0A0H3PJH9	CtpA, carboxyl-t	9	3	1.64E+05
A0A0H3PAQ1	Cjj81176_0849,	2	1	1.57E+05
A0A0H3PC06	Cjj81176_0400,	11	2	1.50E+05
A0A0H3PJE1	Cjj81176_0214,	5	1	1.31E+05
A0A0H3P9Y0	Cjj81176_1228,	2	2	1.21E+05
A0A0H3P9H6	Cjj81176_0967,	5	1	9.57E+04

A0A0H3PBM4	Cjj81176_0677,	21	2	8.29E+04
A0A0H3PBT1	Cjj81176_0149,	2	1	8.24E+04
Q0Q7H1	AtpE, ATP synth	31	2	7.76E+04
A0A0H3PAA9	Cjj81176_1435,	10	5	7.16E+04
A0A0H3PBJ1	KpsE, capsular p	7	2	7.00E+04
A0A0H3P9Y9	Ldh, L-lactate de	5	1	6.99E+04
Q2M5Q6	Cjj81176_1318,	2	1	6.30E+04
A0A0H3PD23	Cjj81176_1105,	15	3	5.26E+04
A1W170	FlgI	9	2	5.02E+04
A0A0H3PE93	LolD, lipoprotein	9	2	4.89E+04
A0A0H3PBA0	CarA, carbamoy	2	1	4.70E+04
A0A0H3PBJ5	DsbC, thiol:disul	5	2	4.23E+04
Q0Q7I0	Cjj81176_1569,	9	4	3.86E+04
A0A0H3P994	Cjj81176_0144,	6	1	3.72E+04

* These proteins were not detected by mass spectrometry in D*pflA* /vector. Thus, no abundance ratios can be calcualted.

TABLE S2

Protein	Accession number	Functional description	Color in figures	Approx. resolution (d99) cite PMID 30198894	Stoichiometry	Region modelled	Structural source
MotB	A0A0H3P BX6	Stator unit component	Light pink	>10	2 (x17)	15-55 (TM) 68-247 (periplasmic)	From PMID 32931735 AlphaFold2
FliL	A0A0H3PI F6	MotB-associated periplasmic protein	Dark red	>10	4 (x17)	81-178	Homology modelfrom PMID 35046042
PflA	A0A0H3P AU5	Scaffold protein that recruits PflB	Light green	9.1	1 (x17)	16-788	AlphaFold2
PflB	A0A0H3P J87	Scaffold protein that recruits stator complexes by MotB	Dark green	>10	1 (x17)	138-820	AlphaFold2

PflC	A0A0D7VI M6	Scaffold protein that attaches the scaffold to the basak disk, makes up the medial disk	Magenta, teal	9.3 - 9.7	1 (x17)+ 6 (x17)	16-364	AlphaFold2
PflD	A0A0H3P AU1	Scaffold protein	Black	>10	1 (x17)	91-162	AlphaFold2
FlgP	A0A0H3P CP8	Makes up the basal disk, a large rigid OM-asociated brace	Purple	9.9	51	66-171	AlphaFold2

TABLE S3

REAGENT or RESOURCE	SOURCE	IDENTIFIER
Antibodies		
FlgP specific antisera	Ref[21]	FlgP specific antisera
Anti-GFP	Roche	#11814460001, RRID:AB_390913
Anti-FLAG	Sigma-Aldrich	#F1804-1MG, RRID:AB_262044
Anti-mouse IgG	GE Healthcare	#RPN4201
Anti-rabbit IgG	GE Healthcare	#RPN4301
Bacterial and virus strains		
C. jejuni 81-176 *rpsl*^{Sm} (Sm^{R})	Ref[53]	*C. jejuni* DRH212
C. jejuni 81-176 Δ*flhG* Δ*flaAB*	This work	*C. jejuni* minicell-producing strain
C. jejuni 81-176 *pflA*$_{\Delta 18\text{-}168}$	This work	*C. jejuni* PflA truncation
C. jejuni NCTC11168 wildtype	This work	*C. jejuni* NCTC11168 WT CSS-0032
C. jejuni NCTC11168 Δ*cj1643*	This work	*C. jejuni* PflC deletion CSS-4087
C. jejuni NCTC11168 Δ*cj0892c*	This work	*C. jejuni* PflD deletion CSS-4081
C. jejuni NCTC11168 Cj1643-3xFLAG	This work	*C. jejuni* PflC-3xFLAG CSS-4720
C. jejuni NCTC11168 Δ*cj0892c* + *cj0892c-sfgfp*	This work	*C. jejuni* PflD-sfGFP CSS-4666
C. jejuni NCTC11168 Δ*cj0892c* + *cj0892c-sfgfp* , PflA-3xFLAG	This work	*C. jejuni* PflD-sfGFP, PflA-3xFLAG CSS-5714
C. jejuni NCTC11168 Δ*cj0892c* + *cj0892c-sfgfp* , PflB-3xFLAG	This work	*C. jejuni* PflD-sfGFP, PflB-3xFLAG CSS-5716
C. jejuni 81-176 Δ*flgQ / pDRH7476*	This work	*C. jejuni* FlgQ-mCherry DRH7516
E. coli DH5α	Lab stock	Cloning strain
E. coli BL21(DE3)	Lab stock	Protein expression strain
C. jejuni 81-176 *rpsL*^{Sm} Δ*pflA*	Ref[9]	*C. jejuni* DAR1124
C. jejuni 81-176 *rpsL* Δ*pflA/pDAR3417*	This work	*C. jejuni* DAR3447

C. jejuni 81-176 *rpsL* *ΔpflA/pDAR1604*	This work	*C. jejuni* DAR3477
C. jejuni 81-176 *rpsL* ^{Sm} *ΔpflB*	Ref[9]	*C. jejuni* DAR981
C. jejuni 81-176 *rpsL* *ΔpflB/pDAR3414*	This work	*C. jejuni* DAR3451
C. jejuni 81-176 *rpsL* *ΔpflB/pDAR965*	This work	*C. jejuni* DAR3479
C. jejuni 81-176 Δ*flaA* *flaB* ^{S397} *flhF* ^{D321A}Δ*cheY*	This work	CCW-locked *C. jejuni* with subpolar short filaments for bead assay
C. jejuni 81-176 *rpsL* Δ*flgX/pDRH8743*	This work	DRH8754
Deposited data		
Raw single particle analysis movies	This work	EMPIAR-11580 (DOI: 10.6019/EMPIAR-10016)
Whole motor map	This work	EMD-16723
Lathed LP-ring focused refinement map	This work	EMD-16723 (additional volume)
Lathed C-ring focused refinement map	This work	EMD-16723 (additional volume)
Lathed MS-ring focused refinement map	This work	EMD-16723 (additional volume)
Focused periplasmic scaffold map	This work	EMD-16724
Δ*pflC* subtomogram average	This work	EMD-17415
Δ*pflD* subtomogram average	This work	EMD-17416
pflA $_{\Delta 16\text{-}168}$ subtomogram average	This work	EMD-17417
FlgQ-mCherry subtomogram average	This work	EMD-17419
C-ring subtomogram average	This work	EMD-19642
Recombinant DNA		

Source of *cat* cassette for chloramphenicol resistance	Ref[81]	pRY109
E. coli-C. jejuni shuttle vector	Ref[81]	pRY112
pRY112 with 76-bp fragment containing *cat* promoter with start codon and in- frame BamHI restriction site cloned into the XbaI and XmaI sites	This work	pDAR1003
pDAR1003 with DNA encoding *mcherry* and stop codon cloned in-frame with respect to the *cat* start codon and BamHI site into the XmaI and EcoRV sites	This work	pDAR1006
Fusion with *flgQ* from codon 2 to the penultimate codon cloned into the BamHI site of pDAR1006 to create a FlgQ-mCherry fusion	This work	FlgQ-mCherry plasmid pDRH7476
E. coli-C. jejuni shuttle vector	Ref[81]	pRY108
E. coli-C. jejuni shuttle vector containing cat promoter and start codon for expression of genes for complementation	Ref[82]	pECO102
E. coli-C. jejuni shuttle vector containing cat promoter and start codon followed by DNA encoding an in-frame N-terminal FLAG tag	Ref[78]	pDAR965
pRY108 with 206 base pair fragment containing flaA promoter and start codonwith in-frame SpeI site cloned into the XbaI and BamHI sites	This work	pDAR1425

E. coli-C. jejuni shuttle vector containing flaA promoter and start codon followed by DNA encoding an in-frame N-terminal FLAG tag	Ref[83]	pDAR1604
pECO102 with codon 2 to penultimate codon of pflB and an in-frame C-terminal FLAG epitope cloned into the BamHI site	This work	pDAR3414
pDAR1425 with codon 2 to penultimate codon of pflA and an in-frame C-terminal FLAG epitope cloned into the BamHI site	This work	pDAR3417
pECO102::*flgX-lysozyme*	This work	pDRH8743
pLIC-PflA	This work	Full-length PflA (16-788)
pLIC-PflAα	This work	PflA TPR regions (169-788)
pLIC-$PflA_N$	This work	PflA N-terminal half (16-454)
pLIC-PflB	This work	Soluble PflB (113-820)
pLIC-PflC	This work	Full-length PflC (17-364)
pLIC-$PflC_{\Delta 236-349}$	This work	PflC C-terminal truncation (17-235)
pLIC (Amp^R)	Franziska Sendker	Cloning vector backbone